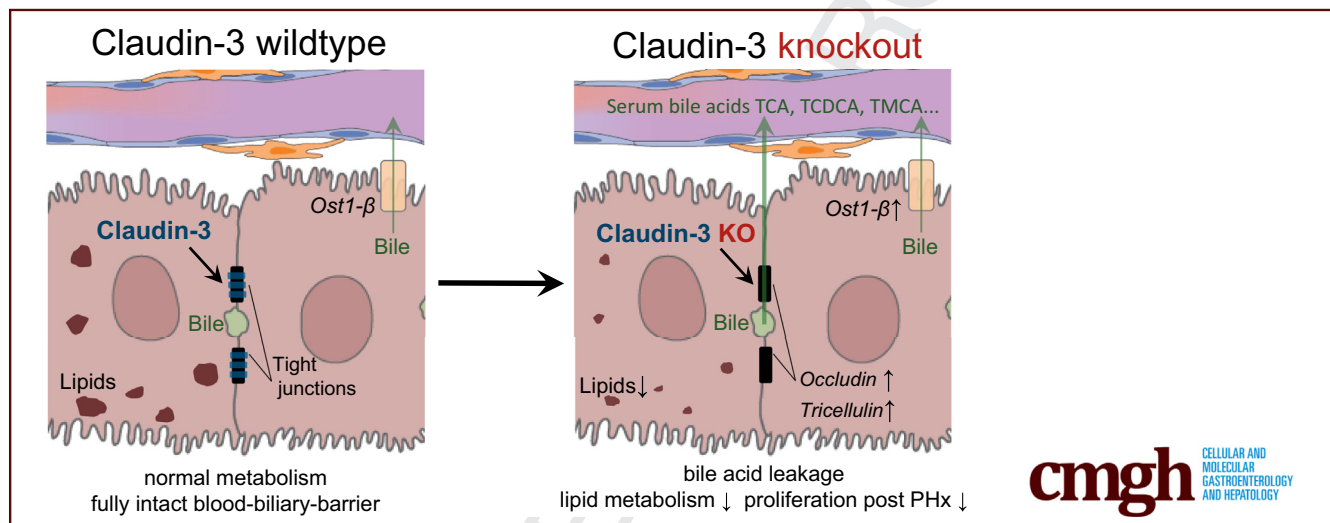


ORIGINAL RESEARCH

Loss of Claudin-3 Impairs Hepatic Metabolism, Biliary Barrier
Function, and Cell Proliferation in the Murine Liver

Felix Alexander Baier,¹ Daniel Sánchez-Taltavull,¹ Tural Yarahmadov,¹ Cristina Gómez Castellà,² Fadi Jebbawi,² Adrian Keogh,¹ Riccardo Tombolini,¹ Adolfo Odriozola,³ Mariana Castro Dias,⁴ Urban Deutsch,⁴ Mikio Furuse,⁵ Britta Engelhardt,⁴ Benoît Zuber,³ Alex Odermatt,² Daniel Candinas,¹ and Deborah Stroka¹

¹Visceral Surgery and Medicine, Inselspital, Bern University Hospital, Department for BioMedical Research, ³Institute of Anatomy, ⁴Theodor Kocher Institute, University of Bern, Bern, Switzerland; ²Division of Molecular and Systems Toxicology, Department of Pharmaceutical Sciences, University of Basel, Basel, Switzerland; ⁵Division of Cell Structure, National Institute for Physiological Sciences, Okazaki, Japan



SUMMARY

Delineating the cell type-specific expression of hepatic tight junction genes showed that claudin-3 is the predominant tight junction protein on hepatocytes and cholangiocytes. In vivo study of claudin-3 knockout mice showed that claudin-3 is necessary to maintain lipid metabolism, biliary-barrier function, and optimal liver regeneration.

BACKGROUND & AIMS: Tight junctions in the liver are essential to maintain the blood-biliary barrier, however, the functional contribution of individual tight junction proteins to barrier and metabolic homeostasis remains largely unexplored. Here, we describe the cell type-specific expression of tight junction genes in the murine liver, and explore the regulation and functional importance of the transmembrane protein claudin-3 in liver metabolism, barrier function, and cell proliferation.

METHODS: The cell type-specific expression of hepatic tight junction genes is described using our mouse liver single-cell sequencing data set. Differential gene expression in *Cldn3*^{-/-} and *Cldn3*^{+/+} livers was assessed in young and aged mice by RNA sequencing (RNA-seq), and hepatic tissue was analyzed for

lipid content and bile acid composition. A surgical model of partial hepatectomy was used to induce liver cell proliferation.

RESULTS: Claudin-3 is a highly expressed tight junction protein found in the liver and is expressed predominantly in hepatocytes and cholangiocytes. The histology of *Cldn3*^{-/-} livers showed no overt phenotype, and the canalicular tight junctions appeared intact. Nevertheless, by RNA-seq we detected a down-regulation of metabolic pathways in the livers of *Cldn3*^{-/-} young and aged mice, as well as a decrease in lipid content and a weakened biliary barrier for primary bile acids, such as taurocholic acid, taurochenodeoxycholic acid, and taurine-conjugated muricholic acid. Coinciding with defects in the biliary barrier and lower lipid metabolism, there was a diminished hepatocyte proliferative response in *Cldn3*^{-/-} mice after partial hepatectomy.

CONCLUSIONS: Our data show that, in the liver, claudin-3 is necessary to maintain metabolic homeostasis, retention of bile acids, and optimal hepatocyte proliferation during liver regeneration. The RNA-seq data set can be accessed at: <https://www.ncbi.nlm.nih.gov/geo/query/acc.cgi?acc=GSE159914> (token: wrmhoaccjrgrijyz). (*Cell Mol Gastroenterol Hepatol* 2021;■:■-■; <https://doi.org/10.1016/j.jcmgh.2021.04.003>)

Keywords: Tight Junction; Bile Acid; Liver Regeneration; Claudin; Single-Cell RNA Sequencing.

Tight junction (TJ) proteins can be found in almost every organ of the body, where their primary function is to create a semipermeable paracellular barrier that restricts passage of ions and solutes.¹ TJ protein expression is highly organ-specific.^{2,3} In the liver, TJs act as a separator of bile and blood circulation in hepatocytes and cholangiocytes.⁴ The molecular components of hepatic TJs comprise a number of different transmembrane and cytoplasmic proteins that have varying expression intensity and localization within the tissue.⁴ Thus far, the cell type-specific expression of hepatic TJ proteins has remained largely unexplored.

The protein family that best defines the barrier and sealing properties of a TJ are the claudins.⁵ Claudins are transmembrane proteins that have 27 known family members in human beings.⁶ Structurally, claudins consist of 4 transmembrane segments, 2 extracellular loops, and 1 intracellular loop, with the N-terminus and C-terminus facing the cytosol. The C-terminal end also harbors the PDZ binding motif, which is the binding site for other proteins of the TJ complex.⁷⁻⁹ The extracellular loops of some claudins may serve as binding sites for hepatitis C virus or *Clostridium perfringens* enterotoxin.¹⁰⁻¹³ Sealing-type claudin-1, -3, -5, -11, -14, and -19 form a tightly closed paracellular barrier, whereas the pore-forming claudin-2, -10a/b, -15, -17, and -21 enable the selective passage of ions and solutes.^{6,14,15} Previous reports have shown that claudins of both sealing and pore-forming types can be found in liver tissue.⁴ Mutations and/or abnormal expression of claudin proteins is associated with multiple hepatic morbidities such as hepatomegaly, jaundice, portal hypertension, restricted bile flow, or cirrhosis.¹⁶⁻¹⁹ For example, absence of sealing claudin-1 may cause the rare genetic disease neonatal ichthyosis and sclerosing cholangitis, in which patients present with cholestasis and increased serum levels of γ -glutamyltransferase, transaminase activity, and bilirubin.^{16,17} Knockout of pore-forming claudin-2 on the other hand reduces bile flow and concentrates lipids and acids within the hepatic bile of mice.¹⁸ Claudin-3 is another sealing-type claudin^{20,21} that controls the barrier for calcium phosphate ions.²² Intestinal studies have shown that claudin-3 expression changes in high-fat or inflammatory environments, suggesting a role for metabolic regulation.²³⁻²⁵ Until now, it was not known if claudin-3 contributed to liver lipid metabolism or regenerative recovery after tissue loss.

Using data from single-cell RNA sequencing, we delineate the cell type-specific TJ gene expression of a mouse liver. We identified *Cldn3* as one of the most abundant transmembrane TJ genes in the liver with expression in hepatocytes and cholangiocytes. Using *Cldn3*^{-/-} mice, we found that claudin-3 is essential for the liver's metabolic homeostasis and that loss of claudin-3 impairs hepatocyte proliferation after partial hepatectomy (PHx).

Results

Expression Profile of TJ Genes in Hepatic Cells

To describe the hepatic expression of TJ genes, we used our recently published single-cell RNA sequencing (scRNA-seq) data set of parenchymal and nonparenchymal cells from a C57BL/6 liver.²⁶ Unsupervised clustering identified 14

unique cell clusters (Figure 1A). A defined set of marker genes and clustering for cell classification identified the populations of hepatocytes, cholangiocytes, endothelial cells, immune cells, and stellate cells (Figure 1B). Expression of TJ genes within these 5 populations is shown in the heatmap, with hepatocytes expressing *Cldn3*, *Cldn5*, *Cldn12*, *Jam-a*, and *Pard3*. Cholangiocytes expressed high levels of *Cldn3*, *Cldn6*, *Cldn7*, and *Jam-a*. Endothelial and stellate cells expressed mostly *Cldn5*, but also *Jam-a*, *Jam-b*, and others. TJ messenger RNA (mRNA) also could be detected in immune cells, including *Cldn5*, *Jam-a*, *Sympk*, and *Ybx3* (Figure 1C). Some TJ genes, such as *Jam-a* and *Ybx3*, were expressed over several cell populations. We observed that *Cldn3* is the TJ gene with the highest mRNA expression in hepatocytes and cholangiocytes (Figure 1C and D). Confocal Z-stack imaging showed that claudin-3 protein was localized with particularly high abundance at the hepatocyte canalicular membrane (Figure 1E and Supplementary Video 1) and had strong expression on the luminal membranes of cholangiocytes (Figure 1F). By immunofluorescence, we observed that claudin-3 protein has a zoned expression pattern in the liver, with the highest staining intensity in the pericentral region (Figure 1G). In summary, our scRNA-seq and immunofluorescence data show that claudin-3 is a prominent hepatic TJ protein that is found predominantly on canalicular membranes of pericentral hepatocytes and on the membranes of ductular cholangiocytes.

Effect of Claudin-3 Deletion on Liver Histology and TJ Integrity

We next assessed if claudin-3 contributes to normal liver homeostasis and function by studying mice with global claudin-3 knockout.²⁷ We first verified that *Cldn3*^{-/-} mice had no claudin-3 protein expression and confirmed the specificity of the claudin-3 antibody by Western blot and by immunostaining of liver tissue (Figure 2A and B). The livers of *Cldn3*^{-/-} mice had no macroscopic anatomic abnormalities (Figure 2C) and the liver's histology was unremarkable compared with age-matched littermate controls (Figure 2D). Furthermore, we could not detect gaps or discontinuities at TJs by electron microscopy (Figure 2E). There was also no difference in collagen deposition in male compared with female *Cldn3*^{-/-} livers (Figure 2F and G). Serum analysis showed no difference in alanine aminotransferase (ALT) and aspartate aminotransferase (AST) levels, but slightly higher levels of alkaline phosphatase (ALP) in *Cldn3*^{-/-} livers, with 142.3 ± 15.8 U/L compared with 117.8 ± 23.3 U/L in *Cldn3*^{+/+} livers (Figure 2H). It has been described that loss

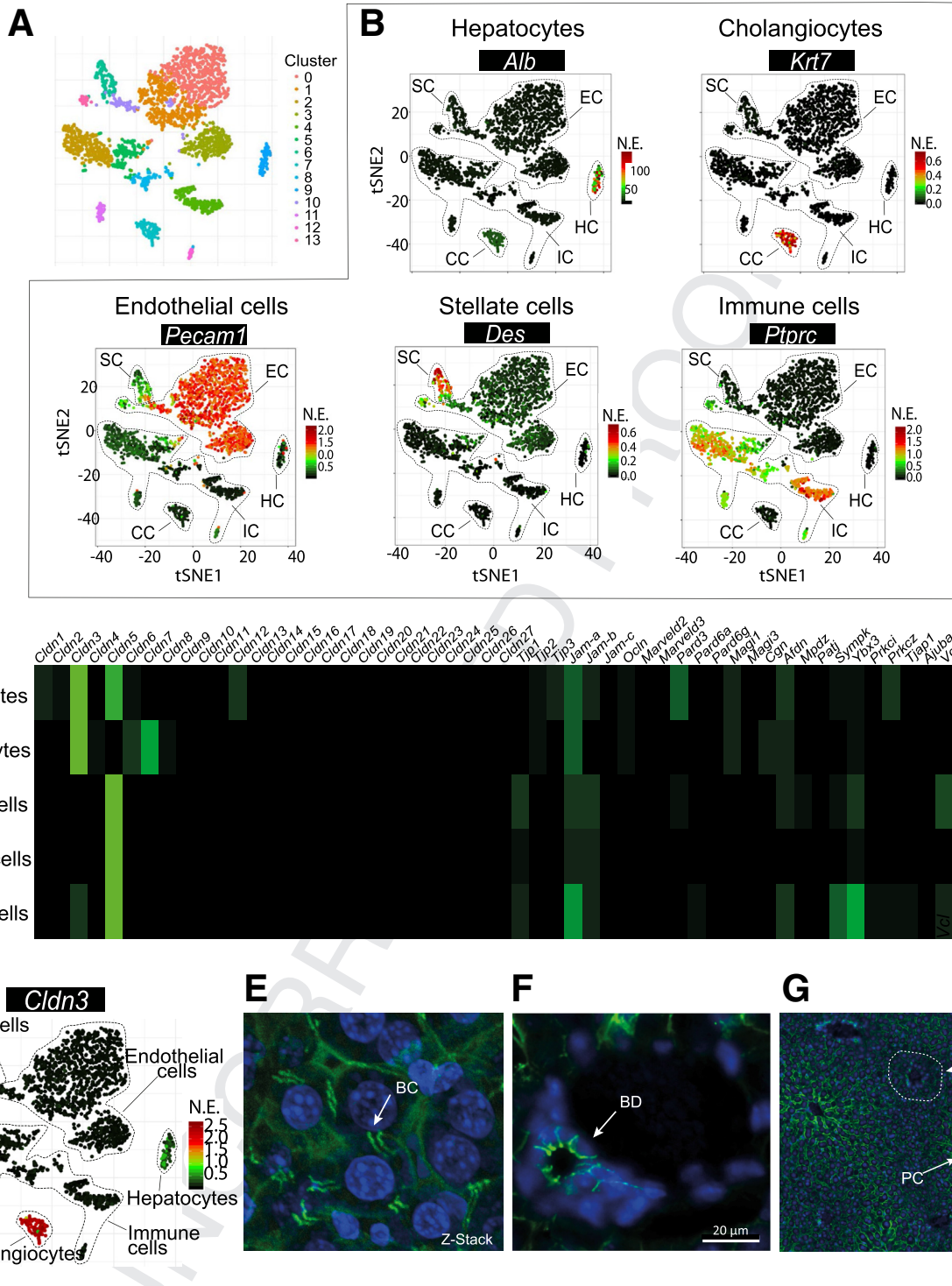
Abbreviations used in this paper: ALP, alkaline phosphatase; ALT, alanine-aminotransferase; AST, aspartate-aminotransferase; CA, cholic acid; DAPI, 4',6-diamidino-2-phenylindole; mRNA, messenger RNA; PBS, phosphate-buffered saline; pHH3, phosphohistone H3; PHx, partial hepatectomy; qPCR, quantitative polymerase chain reaction; scRNA-seq, single-cell RNA sequencing; TCA, taurocholic acid; TJ, tight junction; UMI, unique molecular identifiers.

© 2021 The Authors. Published by Elsevier Inc. on behalf of the AGA Institute. This is an open access article under the CC BY-NC-ND license (<http://creativecommons.org/licenses/by-nc-nd/4.0/>).

2352-345X/\$36.00

<https://doi.org/10.1016/j.jcmgh.2021.04.003>

235
236
237
238
239
240
241
242
243
244
245
246
247
248
249
250
251
252
253
254
255
256
257
258
259
260
261
262
263
264
265
266
267
268
269
270
271
272
273
274
275
276
277
278
279
280
281
282
283
284
285
286
287
288
289
290
291
292
293

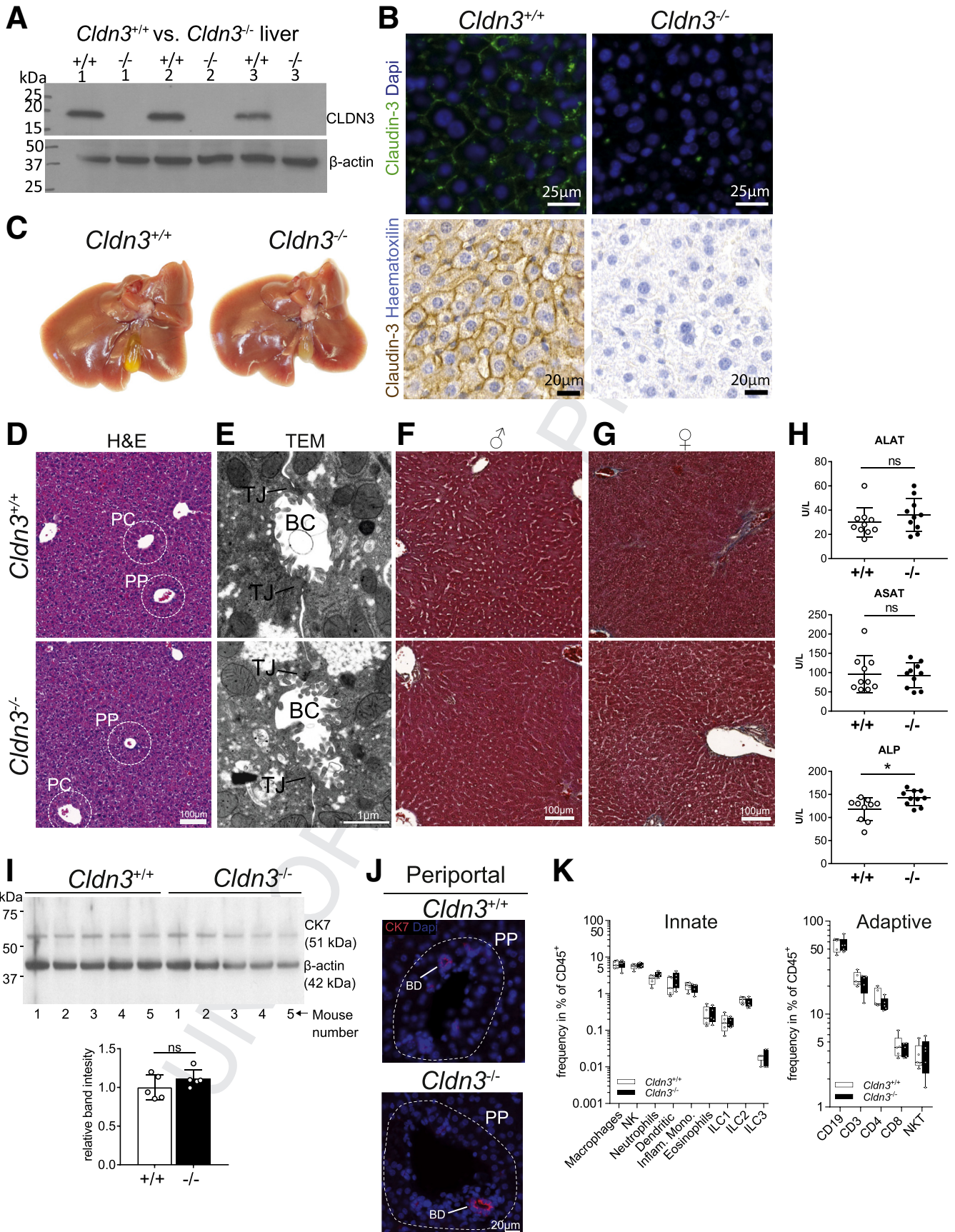


294
295
296
297
298
299
300
301
302
303
304
305
306
307
308
309
310
311
312
313
314
315
316
317
318
319
320
321
322
323
324
325
326
327
328
329
330
331
332
333
334
335
336
337
338
339
340
341
342
343
344
345
346
347
348
349
350
351
352

Figure 1. Cell type-specific analysis of TJ gene expression in a native mouse liver shows high expression of claudin-3 in hepatocytes and cholangiocytes. (A) Unsupervised clustering of the scRNA-seq data used for cell classification. (B) t-Distributed stochastic neighbor embedding (tSNE) plots depicting the expression of marker genes to define different hepatic cell populations: hepatocytes (HC), cholangiocytes (CC), stellate cells (SC), immune cells (IC), endothelial cells (EC). (C) Heatmap of scRNA-seq data depicting cell type-specific expression of hepatic TJ genes. Expression was normalized by cell type. (D) tSNE plot depicting the expression of *Cldn3*. (E) Three-dimensional reconstruction of a 30- μ m-thick confocal z-stack section stained for claudin-3 immunofluorescence (green), DAPI (blue) in mouse liver tissue. (F) Anti-claudin-3 centered on a bile duct. (G) Lower-magnification image showing zoned claudin-3 expression in the murine liver. (E–G) The microscope used for fluorescent image acquisition was a panoramic 250 Flash III, 3DHISTECH, panoramic scanner software, with a 40 \times objective. BC, bile canaliculus; BD, bile duct; NE, normalized expression; PC, pericentral zone; PP, periportal zone.

353
354
355
356
357
358
359
360
361
362
363
364
365
366
367
368
369
370
371
372
373
374
375
376
377
378
379
380
381
382
383
384
385
386
387
388
389
390
391
392
393
394
395
396
397
398
399
400
401
402
403
404
405
406
407
408
409
410
411

412
413
414
415
416
417
418
419
420
421
422
423
424
425
426
427
428
429
430
431
432
433
434
435
436
437
438
439
440
441
442
443
444
445
446
447
448
449
450
451
452
453
454
455
456
457
458
459
460
461
462
463
464
465
466
467
468
469
470



web 4C/FPO

of TJ integrity may cause inflammation and ductular reactions as a result of the cytotoxic effect of bile acid leakage.²⁸ Confirming our observation of intact TJ structures in *Cldn3*^{-/-} livers, we did not observe an increase in CK7, a marker for ductular reactions (Figure 2I and J) or an increase in the frequency of innate or adaptive immune cells in the livers (Figure 2K). In summary, we did not observe any gross alterations in liver histology or signs of loss of TJ integrity in *Cldn3*^{-/-} mice.

Claudin-3 Deletion Represses Metabolism and Bile Synthesis Gene Expression

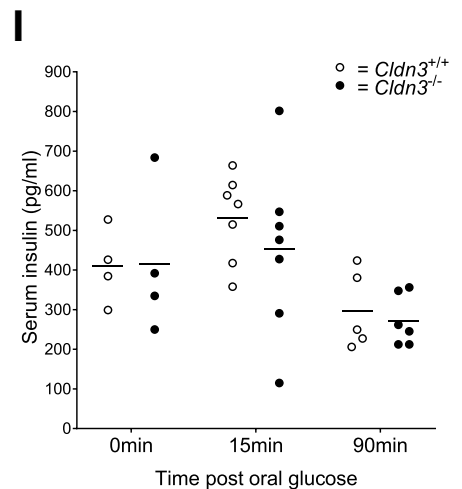
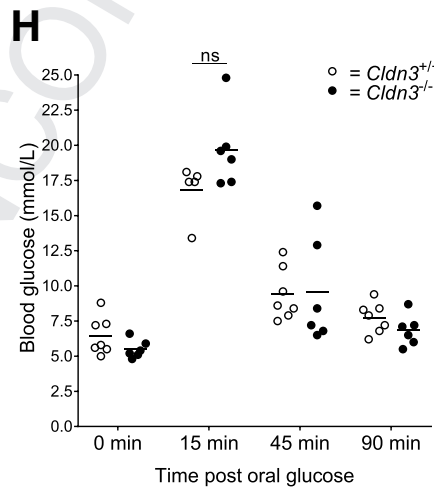
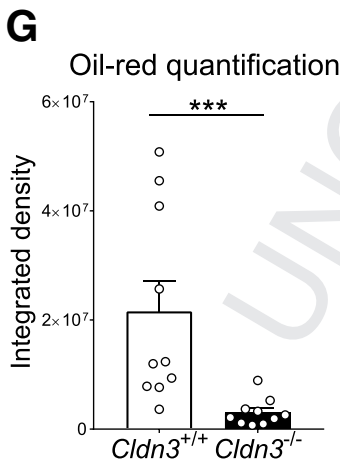
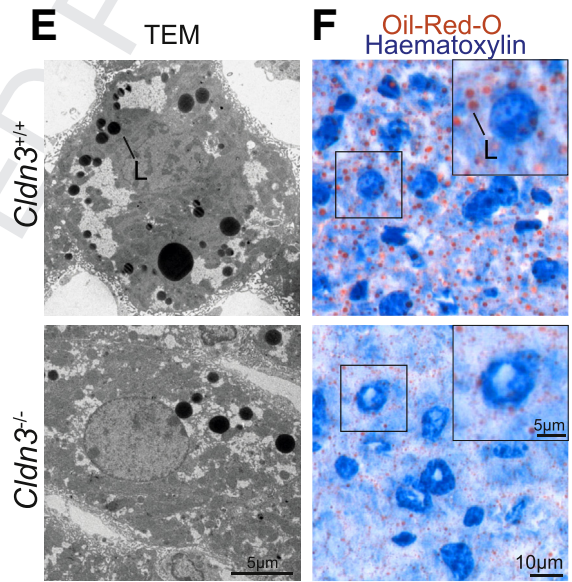
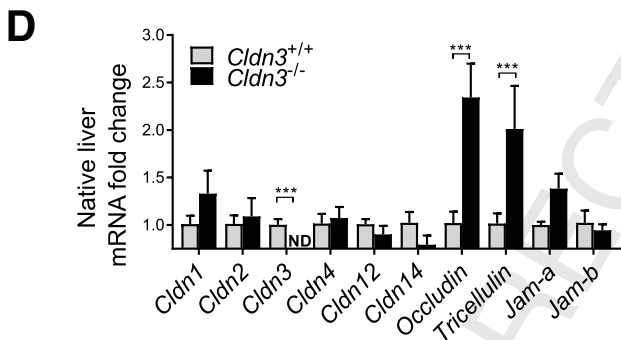
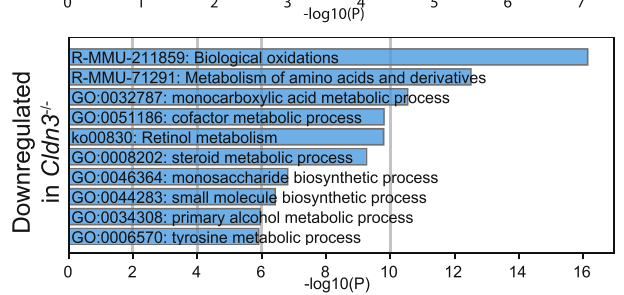
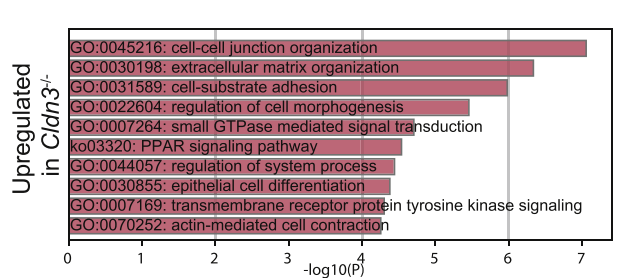
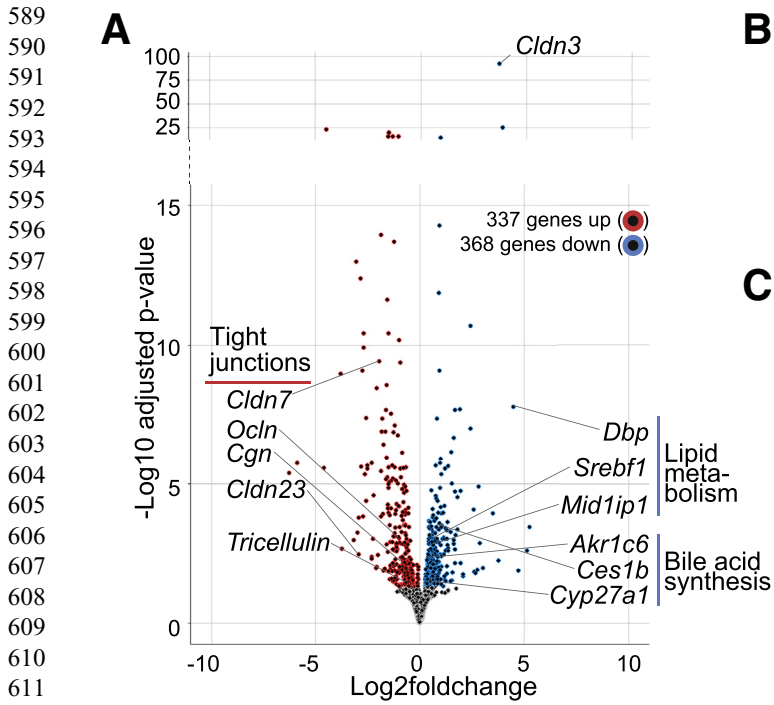
Questioning the absence of an overt phenotype by loss of claudin-3, we next checked if there were any overall changes in gene expression in *Cldn3*^{-/-} livers. RNA-seq analysis showed that there were 705 differentially expressed genes between wild-type and *Cldn3*^{-/-} livers, of which 337 genes were up-regulated, and 368 genes were down-regulated (Figure 3A). Genes related to cell adhesion and cell junctions were up-regulated significantly in *Cldn3*^{-/-} livers, for example, there was higher expression of *Ocln* (Occludin), *Tricellulin* (Marveld2), *Cldn7*, *Cldn23*, and *Cgn* (Figure 3A and B). The most important changes were verified by comparative real-time quantitative polymerase chain reaction (qPCR) (Figure 3D). From the RNA-seq data, we also observed a significant down-regulation of genes and pathways related to metabolism, including fatty acid-, amino acid-, bile acid-, and lipid-related gene expression in *Cldn3*^{-/-} livers (Figure 3A and C). This observation was consistent with the low amount of lipid droplets in *Cldn3*^{-/-} hepatocytes, as seen by electron microscopic and quantified Oil-red-O staining (Figure 3E-G). We next questioned the possible cause for repressed lipid metabolism in *Cldn3*^{-/-} livers. Glucose is one of the main drivers of de novo lipogenesis in the liver, which requires its efficient absorption in the intestine.²⁹ Because past reports have shown that Claudin-3 also is expressed in the intestine,³⁰ we hypothesized that an inefficient baseline glucose absorption within the intestine may explain the down-regulation in lipid metabolism in *Cldn3*^{-/-} mice. However, baseline blood

glucose levels did not differ significantly, and *Cldn3*^{-/-} mice showed a similar absorption and clearance after oral glucose challenge (2 mg/g bodyweight) when compared with *Cldn3*^{+/+} mice (Figure 3H). Accordingly, serum insulin levels were not significantly different between *Cldn3*^{+/+} and *Cldn3*^{-/-} in the oral glucose tolerance test (Figure 3I). Taken together, we observed many deregulated genes in *Cldn3*^{-/-} livers, including a compensatory increase of TJ gene expression and a repressive effect on metabolic processes in the liver.

Effect of Claudin-3 Deletion in Aged Animals

Because we observed a repression of lipid metabolism in *Cldn3*^{-/-} mice, we next questioned how they respond to the metabolic challenge of aging. It has been well described that senescence-related events that come with advanced age lead to increased accumulation of lipids and triglycerides in the liver.³¹⁻³³ We first compared liver tissue of 12-week-old and 52-week-old mice and did not observe a change in hepatic claudin-3 protein levels resulting from age (Figure 4A). The bodyweight of *Cldn3*^{+/+} vs *Cldn3*^{-/-} mice was similar over time, while the liver-to-bodyweight ratio of 52-week-old *Cldn3*^{-/-} mice was slightly higher (Figure 4B and C). Liver damage markers ALT and AST did not differ (Figure 4D), however, we observed the same trend of increased ALP in aged *Cldn3*^{-/-} that was present in young animals (Figures 4D and 2H). In aged mice, there was no difference in collagen deposition owing to loss of claudin-3 expression (Figure 4E). We next compared the transcriptomic profile of young vs aged *Cldn3*^{+/+} and *Cldn3*^{-/-} mice by RNA-seq. In young animals there were differences owing to the loss of claudin-3 expression, however, the metabolic challenge of age was stronger than the effect of the loss of claudin-3 in aged animals (Figure 4F). Analysis of differentially expressed genes showed that in both *Cldn3*^{+/+} and *Cldn3*^{-/-} aged animals there was a profound down-regulation of metabolic pathways including fatty acid metabolism and catabolic processes and an up-regulation of inflammation and immune responses (Figure 4G and H). However, when aged *Cldn3*^{+/+} and *Cldn3*^{-/-} were compared, only a few genes

Figure 2. (See previous page). Effect of claudin-3 loss on liver morphology and TJ structure integrity. Mice with global claudin-3 knockout were generated as described in the Methods section. (A) Anti-claudin-3 Western blot on whole-liver tissue lysates of *Cldn3*^{+/+} and *Cldn3*^{-/-} mice. β -actin for loading control. No claudin-3 was detected in *Cldn3*^{-/-} samples, and only a single specific band was seen in *Cldn3*^{+/+} mice (n = 3). (B) Anti-claudin-3 immunofluorescence (green; DAPI in blue), and immunohistochemistry in *Cldn3*^{+/+} and *Cldn3*^{-/-} liver tissue. Claudin-3 staining was absent in the *Cldn3*^{-/-} samples. (C) Photographs of native *Cldn3*^{+/+} and *Cldn3*^{-/-} livers. (D) H&E staining. (E) Transmission electron microscopy (TEM) images centered on bile canaliculi. (F and G) Masson trichrome staining of female and male liver tissue. (H) Serum AST, ALT, and ALP levels in *Cldn3*^{-/-} vs *Cldn3*^{+/+} mice (n = 10, means \pm SD, * P < .05, unpaired t test). (I) Anti-CK7 Western blot on whole-liver tissue of native *Cldn3*^{+/+} and *Cldn3*^{-/-} mice. Band intensities were normalized to β -actin (n = 5, t test, *Cldn3*^{+/+} band intensities were compared with their group average). (J) Anti-CK7 immunofluorescence (red) in periportal liver tissue, and DAPI in blue. Representative images were taken. Quantification of the Western blot below (n = 5, bars represent means \pm SEM, unpaired t test). (K) Fluorescence-activated cell sorting analysis of innate and adaptive immune cell populations. The frequency of immune cells was not different in *Cldn3*^{+/+} and *Cldn3*^{-/-} native livers (n = 5, unpaired t test). The microscopes used for image acquisition in this figure were an immunofluorescence Leica DMI4000B with a 20 \times objective with Leica advance fluorescence software, and an immunohistochemistry panoramic 250 Flash III, 3DHISTECH, panoramic scanner software, with a 20 \times objective; electron microscopy, Philips CM 12. BC, bile canaliculus; CK7, _____; ILC, _____; Inflam. Mono., inflammatory monocytes; NK, _____; NKT, _____; PC, pericentral area; PP, periportal area.



were significantly different, particularly *Apol9a*, *Apol9b*, and *Cyp26a1*, genes related to cholesterol and lipid metabolism, which were lower in *Cldn3*^{-/-} mice (Figure 4J).

Following results from our RNA-seq data and reports that age leads to impaired lipid metabolism,³¹⁻³³ we were able to confirm a significant increase of lipid content in aged livers, however, *Cldn3*^{-/-} mice had a lower lipid content compared with *Cldn3*^{+/+} mice (Figure 4J) as we observed previously in young animals (Figure 3E-G). For further validation of the inflammatory phenotype that our gene expression data indicated (Figure 4G and H), we showed that the frequency of total hepatic lymphocytes increased with age in both groups (Figure 4K). In summary, all aged animals had higher amounts of hepatic lipids and liver inflammation compared with young animals, and aged *Cldn3*^{-/-} mice retained lower hepatic lipid levels compared with wild-type controls.

Impairment of the Blood-Biliary Barrier in *Cldn3*^{-/-} Livers

Our RNA-seq analysis showed that genes involved in bile acid metabolism such as *Cyp27a1*, *Ces1b*, and *Akr1c6* were down-regulated in *Cldn3*^{-/-} mice (Figure 3A). We therefore questioned if there are lower bile acid levels in *Cldn3*^{-/-} mice by measuring their abundance in liver tissue and serum by liquid chromatography-tandem mass spectrometry. Lower total bile acid levels were measured in the liver tissue, while total bile acids were higher in the serum of *Cldn3*^{-/-} mice compared with *Cldn3*^{+/+} mice (Figure 5A and B). The proportion of primary bile acids was higher in the serum of *Cldn3*^{-/-} mice (Figure 5B). Importantly, individual bile acids were significantly less concentrated in the liver (Figure 5C), and more highly concentrated in the serum (Figure 5D). This included cholic acid (CA), taurocholic acid (TCA), taurochenodeoxycholic acid, conjugated forms of muricholic acids and the secondary bile acid tauro-7-oxolithocholic acid (Figure 5C and D). The other individual bile acids did not significantly differ between *Cldn3*^{+/+} and *Cldn3*^{-/-} in the liver or serum (Figure 5E and F). The change in bile composition prompted us to check the appearance of the gallbladders. We did not find any incidence of gallstones in the gallbladders and observed that *Cldn3*^{-/-} gallbladders were lighter in color compared with wild-type organs

(Figure 6A). As a possible contributing factor to the change in circulating bile acid composition, we checked in the RNA-seq data if the expression of transporters is altered in *Cldn3*^{-/-} mice (Figure 6B). The expression of transporter transcripts that showed a trend in the RNA-seq results were verified by real-time qPCR (Figure 6C). We observed higher expression of *Ost1-β* (Slc51b), and a trend for higher *Asbt* (Slc10a2) levels in *Cldn3*^{-/-} mice (Figure 6B and C). Because the nuclear transcription factor Farnesoid X-receptor is a regulator of bile transporters,³⁴ we checked *Fxr* and downstream target expression (Figure 6D). However, we found only a modest alteration of the Farnesoid X-receptor targets *Bacs* (Slc27a5) and *Apoa1* (Figure 6D). Finally, we tested the expression of *Fgf15* in the ileum (Figure 6E), but did not observe a difference in *Cldn3*^{-/-} when compared with *Cldn3*^{+/+} animals. In conclusion, our results suggest that the biliary barrier of *Cldn3*^{-/-} mice is partially impaired and alterations in bile acid transporter expression also may contribute to the change in hepatic bile acid levels.

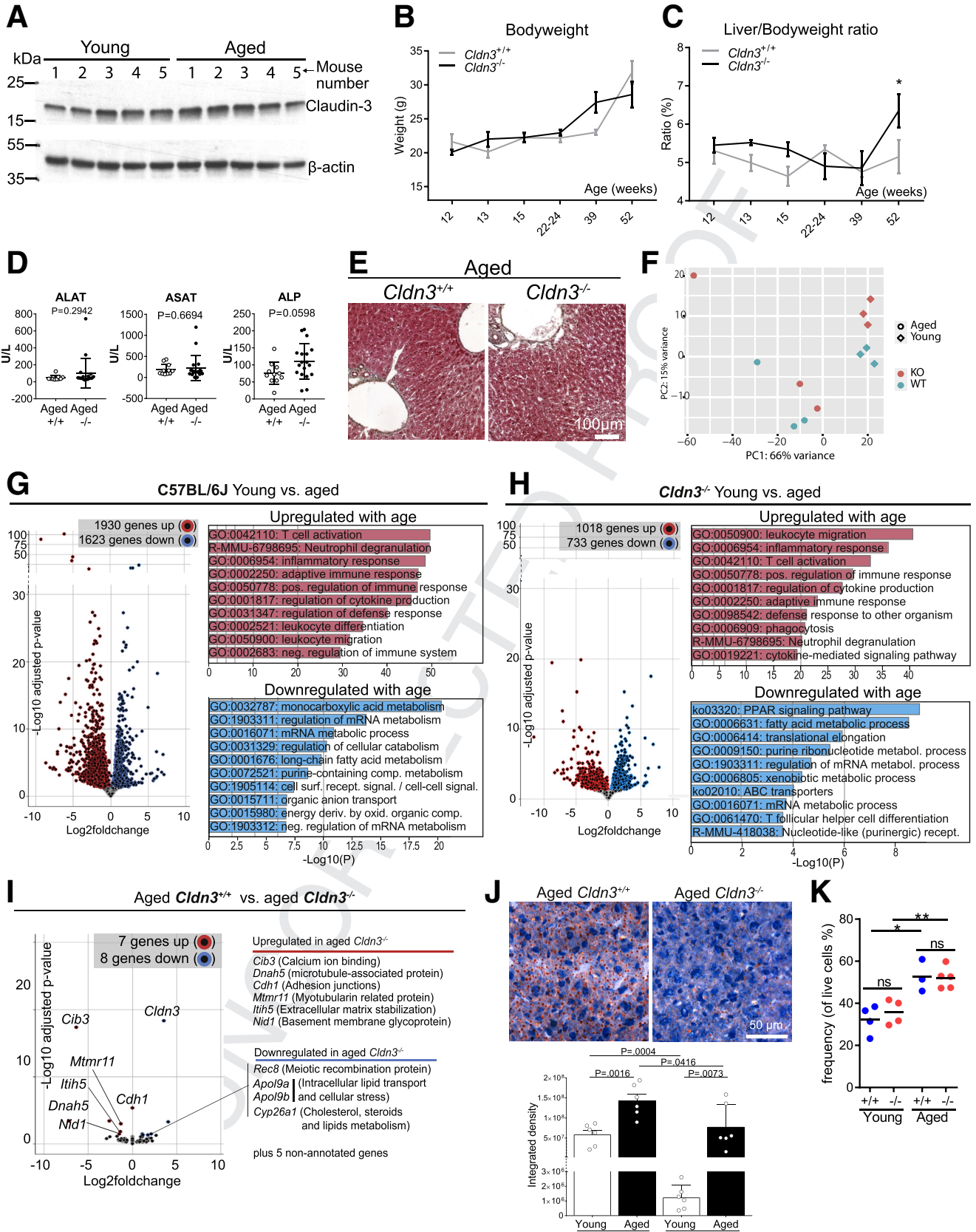
Hepatic Proliferation Is Impaired in *Cldn3*^{-/-} Mice After Partial Hepatectomy

The observations that loss of claudin-3 expression affects liver metabolism, particularly lipid metabolism and hepatic bile acid content, raised the question of whether claudin-3 is important for the liver's response to injury. Therefore, we tested if the loss of claudin-3 expression altered the liver's ability to regenerate after PHx. We observed a time-dependent regulation of claudin-3 mRNA and protein in wild-type animals in response to PHx. *Cldn3* expression was decreased after 3 and 6 hours and increased above baseline levels starting at 24 hours (Figure 7A). We validated this observation by immunofluorescent staining (Figure 7B) and Western blot (Figure 7C and D). The zoned expression pattern that was present in native liver tissue was lost at 48 hours after PHx (Figure 7B). PHx leads to high pressure and mechanical stress within the first hours after resection,³⁵ therefore, we checked if the increased stress affected the integrity of TJs in *Cldn3*^{-/-} mice. However, by electron microscopy, we did not find any gaps or other obvious membrane impairments after 6 hours after PHx in either *Cldn3*^{+/+} or *Cldn3*^{-/-} (Figure 7E). In agreement, there were no signs of an inflammatory reaction based on

Figure 3. (See previous page). Repressed lipid metabolism in *Cldn3*^{-/-} mice. (A) Volcano plot showing up-regulated and down-regulated genes (red circles and blue circles, respectively) in *Cldn3*^{-/-} compared with *Cldn3*^{+/+} native liver tissue. RNA-seq analysis was performed by DESeq2 (n = 3 for *Cldn3*^{-/-} and n = 4 for *Cldn3*^{+/+}, differential expression significance threshold: P value adjusted < .05). A total of 15,148 nonsignificantly regulated genes are shown as grey circles. A selection of significantly regulated genes related to TJs, metabolism, or bile synthesis is annotated. Metascape analysis of the (B) top 10 up-regulated and (C) top 10 down-regulated gene pathways within the data set of panel A. (D) Comparative real-time qPCR in native liver tissue. The fold change in mRNA expression of *Cldn3*^{-/-} was obtained by comparison with *Cldn3*^{+/+} mice (n = 4, unpaired t test, ***P < .001, *Cldn3*^{+/+} control $\Delta\Delta\text{CT}$ values = $\Delta\text{CT}(\text{individual})$ minus $\Delta\text{CT}(\text{group average})$, bars represent the means \pm SEM). (E) Transmission electron microscopy (TEM) images of representative hepatocytes. Lipid droplets (L) appeared less in number and size in *Cldn3*^{-/-} hepatocytes. (F) Oil-red-O staining showing a lower amount of lipid droplets (L) in *Cldn3*^{-/-} liver tissue. (G) Quantification of images from randomly chosen regions of Oil-red-O-stained native liver tissue (n = 10, bars represent means \pm SEM, ***P < .001, Mann-Whitney test). (H) Oral glucose tolerance test. D-glucose (2 mg/g bodyweight) was given by oral gavage and blood glucose levels were determined at the indicated times (n = 7 for *Cldn3*^{+/+} and n = 6 for *Cldn3*^{-/-}, exception for t = 15 min *Cldn3*^{+/+} n = 5, unpaired Student t test). (I) Enzyme-linked immunosorbent assay test for serum insulin levels at the indicated times after oral glucose challenge. No significant differences were observed (0 min, n = 4; 15 min, n = 7; 90 min, n = 5 [*Cldn3*^{+/+}] and n = 6 [*Cldn3*^{-/-}], unpaired Student t test). Microscopes used for image acquisition in this figure for Oil-red-O staining: panoramic 250 Flash III, 3DHISTECH, panoramic scanner software, with a 40 \times objective; electron microscopy, Philips CM 12. ND, nondetectable.

825
826
827
828
829
830
831
832
833
834
835
836
837
838
839
840
841
842
843
844
845
846
847
848
849
850
851
852
853
854
855
856
857
858
859
860
861
862
863
864
865
866
867
868
869
870
871
872
873
874
875
876
877
878
879
880
881
882
883

884
885
886
887
888
889
890
891
892
893
894
895
896
897
898
899
900
901
902
903
904
905
906
907
908
909
910
911
912
913
914
915
916
917
918
919
920
921
922
923
924
925
926
927
928
929
930
931
932
933
934
935
936
937
938
939
940
941
942



web 4C/FPO

943 cytokine secretion or CK7 expression (Figure 7F–H), and the
944 frequencies of immune cells were not significantly different
945 in regenerating *Cldn3*^{-/-} livers (Figure 7I).

946 We next determined the proliferative scores 48 hours
947 after PHx. The percentage of Ki67-positive hepatocytes was
948 76% ± 4% in *Cldn3*^{+/+} mice compared with 49% ± 5% in
949 *Cldn3*^{-/-} mice ($P < .01$) (Figure 8A). For the mitosis marker
950 phosphohistone H3 (pHH3), *Cldn3*^{+/+} livers had 32% ± 3%
951 pHH3-positive nuclei, compared with only 15% ± 1% in
952 *Cldn3*^{-/-} livers ($P < .01$) (Figure 8B). Supporting these re-
953 sults, the transcription of *Foxm1* increased 43- ± 3-fold over
954 controls in *Cldn3*^{+/+}, and only 16- ± 2-fold in *Cldn3*^{-/-} livers
955 ($P < .001$) (Figure 8C). Similarly, *Ccnb1* and *Birc5* were
956 significantly less transcribed in *Cldn3*^{-/-} mice at 48 hours
957 after PHx. The proliferation inhibitor *p21* (Cdkn1a), on the
958 other hand, was expressed higher in *Cldn3*^{-/-} mice at 24 and
959 48 hours after PHx ($P < .05$ and $P < .01$, respectively)
960 (Figure 8C). At 72 hours after PHx, the proliferation scores
961 and the expression of genes regulating cell proliferation did
962 not differ between *Cldn3*^{+/+} and *Cldn3*^{-/-} mice. RNA-seq
963 data of liver tissue 48 hours after PHx supported the
964 immunofluorescence and real-time qPCR data (Figure 8D).
965 Genes associated with cell division, cell-cycle regulation,
966 cholesterol synthesis, and glucose metabolism were
967 expressed at a lower level in regenerating *Cldn3*^{-/-} livers
968 (Figure 8D and F), whereas genes related to circadian
969 rhythm, negative regulation of metabolism, lipid catabolism,
970 and calcium ion binding, as well as others, were found to be
971 up-regulated (Figure 8D and E). Taken together, we saw that
972 *Cldn3*^{-/-} mice had an impairment in proliferation after PHx.

973 Discussion

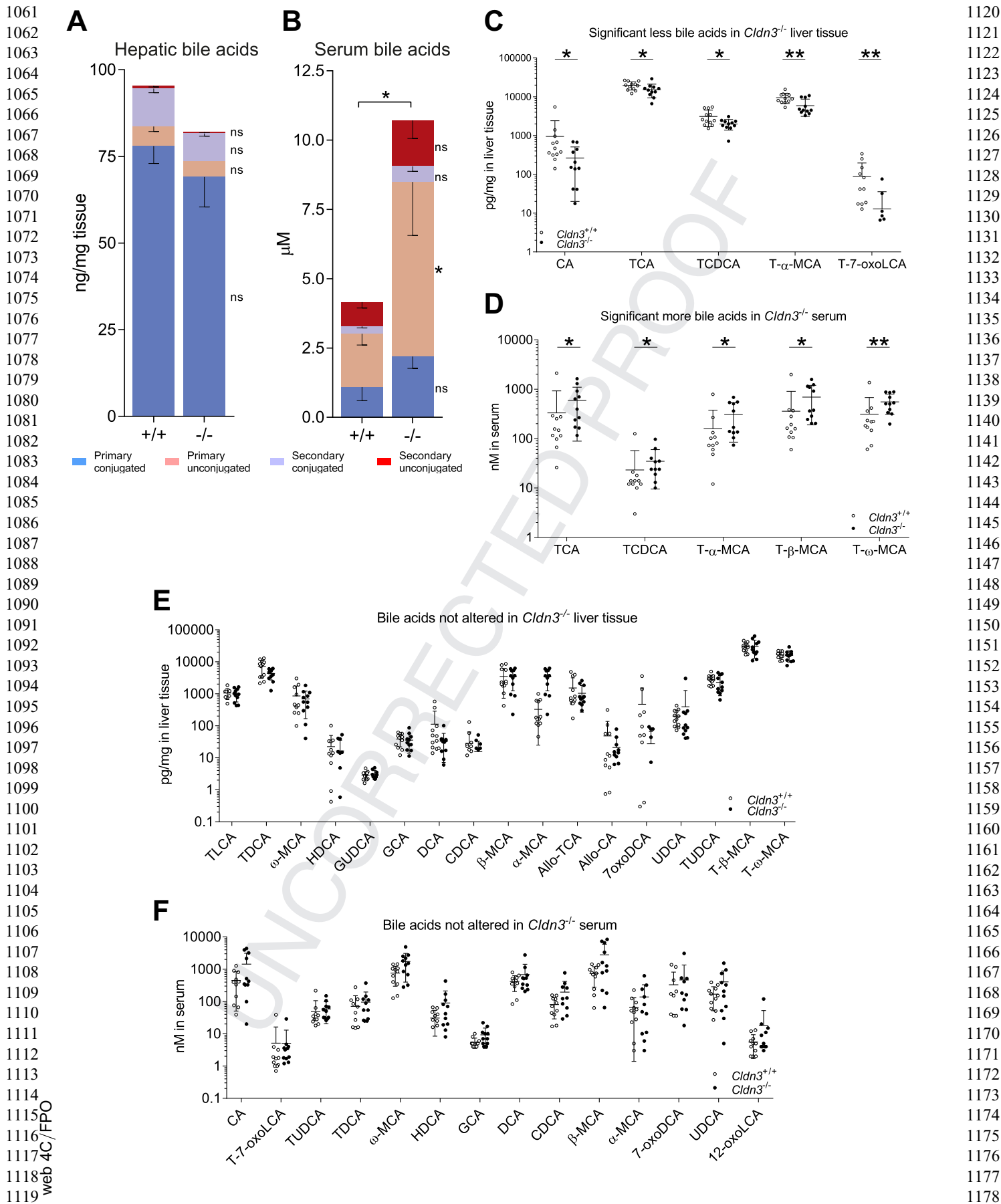
974 Several studies have described hepatic TJ proteins and
975 their function within the blood-biliary barrier.^{4,14,16,18,22} By
976 using scRNA-seq, we expanded the available information on
977 hepatic TJ gene expression by describing their abundance in

the various cell populations of the liver. We found the ex- 1002
pected expression pattern for some genes, for example, 1003
Cldn1, *Cldn2*, *Cldn5*, and *Cldn7*,^{18,36–40} and, interestingly, we 1004
observed expression of *Cldn5*, *Jam-a*, *Jam-b*, *Afdn*, *Sympk*, 1005
and *Ybx3* in stellate and immune cells, suggesting a role of TJ 1006
genes outside the blood-biliary barrier. Our scRNA-seq data 1007
support that *Cldn3* is one of the most highly expressed TJ 1008
genes in the mouse liver with its mRNA and protein 1009
expressed predominantly in hepatocytes and chol- 1010
angiocytes.^{18,22,41–43} Within a liver lobule, there is a 1011
discernable metabolic zonation,^{44,45} and bile acid synthesis 1012
is highest in the first 3 hepatocyte cell layers around the 1013
central veins.⁴⁶ This correlates with the high level claudin-3 1014
expression we observed in the pericentral region, suggest- 1015
ing that the liver may express higher levels of claudin-3 to 1016
ensure a tightly sealed blood-biliary barrier in the location 1017
of higher bile acid concentrations. 1018

To study the consequence of loss of claudin-3 expres- 1019
sion, we used *Cldn3*^{-/-} mice, however, the phenotype we 1020
observed was milder than what was reported originally.²² 1021
For example, in our study, there was a very moderate in- 1022
crease of total serum bile acids and no gallstones were 1023
found even in aged animals.²² A possible explanation could 1024
be differences in environmental factors such as nutrition or 1025
microbiota.⁴⁷ Our transmission electron microscopy images 1026
support that hepatic TJs in *Cldn3*^{-/-} mice are intact because 1027
the membranes of adjacent cells are tightly sealed.²² 1028
Consequently, we could not detect morphologic changes or 1029
signs of inflammation or fibrosis owing to loss of claudin-3 1030
expression. This lack of phenotype may be explained by the 1031
higher expression of other TJ-forming genes such as occlu- 1032
din and tricellulin, which may have functionally compen- 1033
sated for the loss of claudin-3. 1034

However, by sequencing the livers of *Cldn3*^{-/-} mice we 1035
found significant repression in hepatic metabolism. There 1036
was a lower amount of lipid droplets in *Cldn3*^{-/-} livers and 1037
down-regulation of key genes related to lipogenesis 1038

982 **Figure 4. (See previous page). Metabolic challenging by aging leads to lower lipid accumulation in *Cldn3*^{-/-} liver.**
983 (A) Anti-claudin-3 Western blot on whole-liver tissue lysate of young (12 weeks) and aged (52 weeks) wild-type mouse livers. β -
984 actin was used as loading control (n = 5). (B) Body weight measurements in *Cldn3*^{+/+} (gray line) vs *Cldn3*^{-/-} (black line) mice at
985 the indicated age of life (12 weeks, n = 7 [*Cldn3*^{+/+}] and n = 11 [*Cldn3*^{-/-}]; 13 weeks, n = 6 [*Cldn3*^{+/+}] and n = 4 [*Cldn3*^{-/-}]; 15
986 weeks, n = 5 [*Cldn3*^{+/+}] and n = 7 [*Cldn3*^{-/-}]; 22–24 weeks, n = 5; 39 weeks, n = 3 [*Cldn3*^{+/+}] and n = 4 [*Cldn3*^{-/-}], 52 weeks,
987 n = 3 [*Cldn3*^{+/+}] and n = 5 [*Cldn3*^{-/-}]). No significant differences were observed at any age (unpaired *t* test). (C) Liver-to-
988 bodyweight ratio was measured (12 weeks, n = 7 [*Cldn3*^{+/+}] and n = 11 [*Cldn3*^{-/-}]; 13 weeks, n = 6 [*Cldn3*^{+/+}] and n = 4
989 [*Cldn3*^{-/-}]; 15 weeks, n = 5 [*Cldn3*^{+/+}] and n = 6 [*Cldn3*^{-/-}]; 22–24 weeks, n = 5; 39 weeks, n = 3 [*Cldn3*^{+/+}] and n = 4 [*Cldn3*^{-/-}];
990 39 weeks, n = 3; 52 weeks, n = 3 [*Cldn3*^{+/+}] and n = 5 [*Cldn3*^{-/-}]; * $P < .05$, unpaired *t* test). (D) Serum AST, ALT, and ALP levels
991 in mice 1 to 2 years old. *Cldn3*^{-/-} vs *Cldn3*^{+/+} mice (n = 11 for *Cldn3*^{+/+} and n = 18 for *Cldn3*^{-/-}, means ± SD, * $P < .05$,
992 unpaired *t* test). (E) Masson trichrome staining in aged mice. Representative image is shown (n = 3 and n = 4 for *Cldn3*^{+/+} and
993 *Cldn3*^{-/-}, respectively). (F) Principal component analysis plot based on RNA-seq gene expression data of aged (circles) and
994 young (diamonds) *Cldn3*^{+/+} (blue) and *Cldn3*^{-/-} (red) mice (n = 3 for both aged groups, n = 3 for young *Cldn3*^{-/-} and n = 4 for
995 young *Cldn3*^{+/+} group). (G and H) Volcano plots and metascape analysis showing up-regulated and down-regulated genes
996 and the top 10 up-regulated and down-regulated pathways in young (12 weeks) and aged (1.5–2 years) (G) C57BL/6 J mice
997 and (H) *Cldn3*^{-/-} mice. RNA-seq analysis was performed by DESeq2 (n = 3 for both aged groups, n = 3 for young *Cldn3*^{-/-} and
998 n = 4 for young *Cldn3*^{+/+} group, differential expression significance threshold: *P* value adjusted < .05). Genes or pathways
999 with low expression in aged mice are shown in blue, and with high expression in aged mice are shown in red. (I) Volcano plot
1000 showing differential gene expression in aged *Cldn3*^{+/+} vs aged *Cldn3*^{-/-} mice, with regulated genes annotated next to it.
1001 Parameters of the differential gene expression as shown in panels G and H. (J) Oil-red-O staining on liver tissue sections.
Quantification of images from randomly chosen regions below (n = 6, bars represent means ± SD, unpaired *t* test). (K)
Fluorescence-activated cell sorting analysis comparing young and aged *Cldn3*^{+/+} and *Cldn3*^{-/-} mice (n = 4 in young, n = 3 in
aged *Cldn3*^{+/+} and n = 5 in aged *Cldn3*^{-/-}, unpaired *t* test, * $P < .05$, ** $P < .01$). Microscopes used for image acquisition in this
figure: Masson trichrome staining and Oil-red-O staining, panoramic 250 Flash III, 3DHISTECH, panoramic scanner software,
with a 40× objective. KO, knockout; PC, _____; WT, wild-type.



1061
1062
1063
1064
1065
1066
1067
1068
1069
1070
1071
1072
1073
1074
1075
1076
1077
1078
1079
1080
1081
1082
1083
1084
1085
1086
1087
1088
1089
1090
1091
1092
1093
1094
1095
1096
1097
1098
1099
1100
1101
1102
1103
1104
1105
1106
1107
1108
1109
1110
1111
1112
1113
1114
1115
1116
1117
1118
1119

1120
1121
1122
1123
1124
1125
1126
1127
1128
1129
1130
1131
1132
1133
1134
1135
1136
1137
1138
1139
1140
1141
1142
1143
1144
1145
1146
1147
1148
1149
1150
1151
1152
1153
1154
1155
1156
1157
1158
1159
1160
1161
1162
1163
1164
1165
1166
1167
1168
1169
1170
1171
1172
1173
1174
1175
1176
1177
1178

including *Srebf1*.⁴⁸ A main activator of SREBF1 and its downstream targets is glucose.²⁹ We therefore tested if glucose uptake and insulin secretion are affected in *Cldn3*^{-/-} mice, which was not the case. However, we observed decreased expression of bile acid synthesis-involved genes including *Cyp27a1*⁴⁹ and *Akr1c6*.⁵⁰ In combination with the changed composition of the circulating bile acid pool in *Cldn3*^{-/-} mice, it is possible that altered bile metabolism negatively influenced the energy metabolism of the liver, because bile acids are important regulators of lipogenesis.^{51,52} The altered lipid metabolism in *Cldn3*^{-/-} prompted us to question how the mice respond to a metabolic challenge, which we induced by letting the mice age for up to 2 years. Of note, we did not observe a decrease in expression of claudin-3 protein in aged wild-type mice, as previously suggested.⁴³ In aged livers, we observed the expected accumulation of hepatic lipids as well as inflammation and immune cell infiltrations. These events took place in *Cldn3*^{-/-} mice as well. When comparing the gene expression in aged *Cldn3*^{-/-} vs aged *Cldn3*^{+/+} mice by RNA-seq, we found a lower expression of lipid metabolism-related genes *Apol9a/b*⁵³ and *Cyp26a1*⁵⁴ in the knockout animals. In conjunction, we also observed a lower amount of lipids in aged *Cldn3*^{-/-} compared with aged *Cldn3*^{+/+} liver. This implies that *Cldn3*^{-/-} mice respond differently to the metabolic challenge of age, accumulating fewer hepatic lipids. Both *Cldn3*^{+/+} and *Cldn3*^{-/-} mice showed a high lipid and inflammatory phenotype upon metabolic challenge by age, however, aged *Cldn3*^{-/-} mice again showed a phenotype of repressed lipid metabolism.

Because our differential gene expression data showed repression of bile acid synthesis-involved genes including *Cyp27a1*⁴⁹ and *Akr1c6*,⁵⁰ we also questioned if the composition of bile acids differs in *Cldn3*^{-/-} mice. Our results showed that *Cldn3*^{-/-} mice have a reduction in the concentration of hepatic CA, and its conjugated form TCA. In contrast, serum levels of TCA were higher in *Cldn3*^{-/-} mice, and there was a trend toward higher CA serum levels. Similarly, conjugated subtypes of a mouse-specific bile acid, muricholic acid, were decreased in the *Cldn3*^{-/-} liver, and increased in the serum. The cause for the higher amount of serum bile acids could be owing to leaks of TJ barrier that are not visible by electron microscopy, or were owing to the slightly higher expression of the biliary exporter *Ost1-β*. Because bile acids are important for efficient nutrient digestion and lipid uptake,⁵⁵ we may speculate that the change in bile acid composition was a contributing factor to the repression in lipid metabolism of *Cldn3*^{-/-} livers. We next questioned whether the alterations in lipid metabolism and biliary barrier influenced the ability of the liver to

regenerate. In fact, both efficient lipid supply^{56,57} and bile acid accumulation^{49,58} are required to settle the increased energy demand of hepatocytes during cell division. Interestingly, we observed an up-regulation of claudin-3 expression between 24 and 48 hours after PHx, which is in agreement with previous observations made in rats.⁵⁹ The increase of claudin-3 expression suggests that the biliary barrier needs to be tightened at this particular time after surgery. Possibly, claudin-3 retains bile acids to prevent hepatocellular damage, and/or to keep bile acids as liver regeneration-promoting signals.^{58,60,61} Our results showed that cell proliferation was decreased significantly in regenerating *Cldn3*^{-/-} livers, with approximately one-third less Ki67-positive and only half the amount of pHH3-positive cells at 48 hours after PHx. Because liver regeneration has high clinical relevance for treatment of hepatic malignancies and the repair of trauma,^{62,63} our results might be of interest for further investigations on the role of TJ proteins for optimal recovery after tissue loss.

Taken together, our data suggest that loss of claudin-3 leads to an impairment in lipid metabolism and an impaired biliary barrier in mice. Both of these phenotypes likely contribute to the suboptimal hepatic proliferation after PHx. However, we cannot exclude the possibility that claudin-3 is associated with signaling pathways that regulate the cell cycle. For example, claudin-3 is in direct and indirect contact with TJ adapter proteins that are upstream of transcription factors, including ZONAB, C-MYC, β -catenin, YAP, and others.⁶⁴⁻⁶⁷ It will be of future interest to investigate the potential role of claudin-3 in the context of signaling pathways that control cell proliferation.

Materials and Methods

Generation of *Cldn3*^{-/-} Mice

We described the generation of this strain with global claudin-3 knockout in detail in a previous publication.²⁷ In embryonic stem cells, we used a PGK neo cassette to replace most of the claudin-3 coding region, except for the last 30 nucleotides of the ORF. This created a knockout allele and prevented claudin-3 peptide formation, which we confirmed by Western blot and immunofluorescence (Figure 2A and B). By interbreeding heterozygous parents, we created homozygous *Cldn3*^{-/-} mice at almost Mendelian ratios (23.5%). To homogenize the C57BL/6J genetic background, we backcrossed for more than 10 generations.

Animal Housing and PHx Surgery

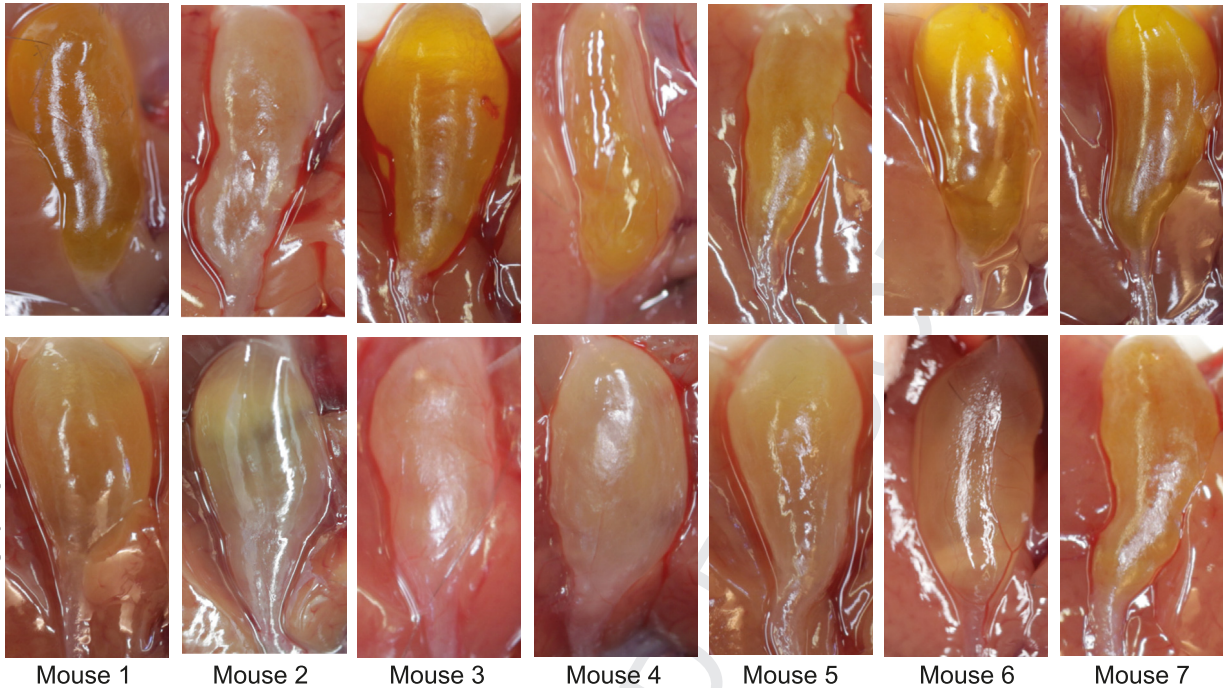
Both experimental C57BL/6J *Cldn3*^{-/-} and control C57BL/6J *Cldn3*^{+/+} mice were born and raised within the

Figure 5. (See previous page). Partial impairment of the *Cldn3*^{-/-} biliary barrier alters bile acid homeostasis. (A) Liquid chromatography–mass spectrometry (LC-MS) analysis of liver bile acids ($n = 12/Cldn3^{+/+}$ and $n = 11/Cldn3^{-/-}$, means \pm SEM, unpaired t test). (B) LC-MS analysis of serum bile acids ($n = 11$, means \pm SEM, $*P < .05$, unpaired t test). (C) LC-MS analysis showing individual bile acid types in the liver ($n = 12/Cldn3^{+/+}$ and $n = 11/Cldn3^{-/-}$, means \pm SD, $*P < .05$, $**P < .01$ Mann-Whitney test). (D) LC-MS analysis showing individual bile acids in the serum ($n = 11$, means \pm SD, $*P < .05$, $**P < .01$ Mann-Whitney test). (E and F) Bile acids that were not changed significantly in *Cldn3*^{+/+} vs *Cldn3*^{-/-} liver tissue or serum ($n = 11$, means \pm SD, Mann-Whitney test). Allo, _____; CDCA, _____; DCA, _____; GCA, _____; GUDCA, _____; HDCA, _____; MCA, _____; oxoLCA, _____; TCDCa, _____; TDCA, _____; TLCA, _____; TUDCA, _____; UDCA, _____.

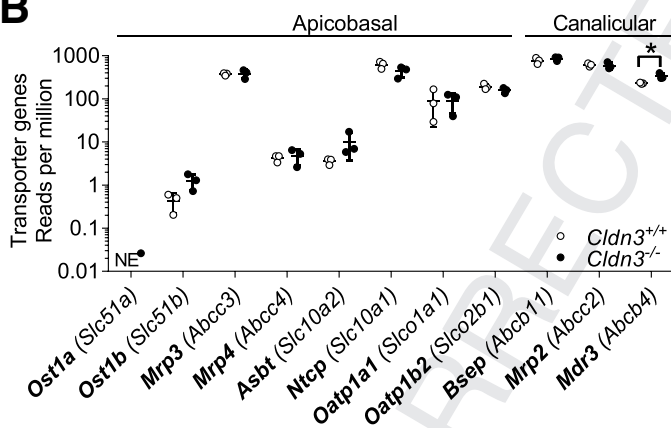
1297
1298
1299
1300
1301
1302
1303
1304
1305
1306
1307
1308
1309
1310
1311
1312
1313
1314
1315
1316
1317
1318
1319
1320
1321
1322
1323
1324
1325
1326
1327
1328
1329
1330
1331
1332
1333
1334
1335
1336
1337
1338
1339
1340
1341
1342
1343
1344
1345
1346
1347
1348
1349
1350
1351
1352
1353
1354
1355

1356
1357
1358
1359
1360
1361
1362
1363
1364
1365
1366
1367
1368
1369
1370
1371
1372
1373
1374
1375
1376
1377
1378
1379
1380
1381
1382
1383
1384
1385
1386
1387
1388
1389
1390
1391
1392
1393
1394
1395
1396
1397
1398
1399
1400
1401
1402
1403
1404
1405
1406
1407
1408
1409
1410
1411
1412
1413
1414

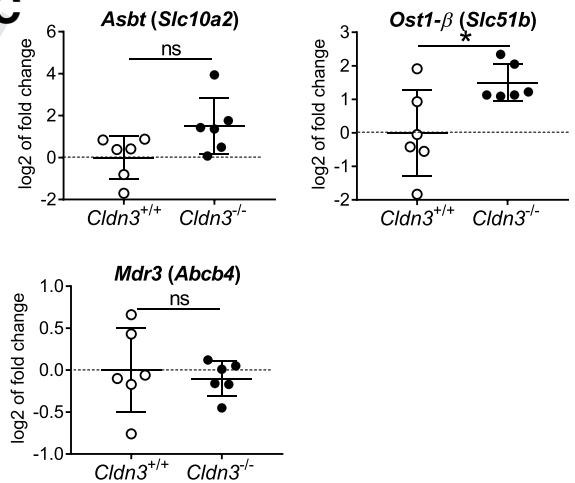
A



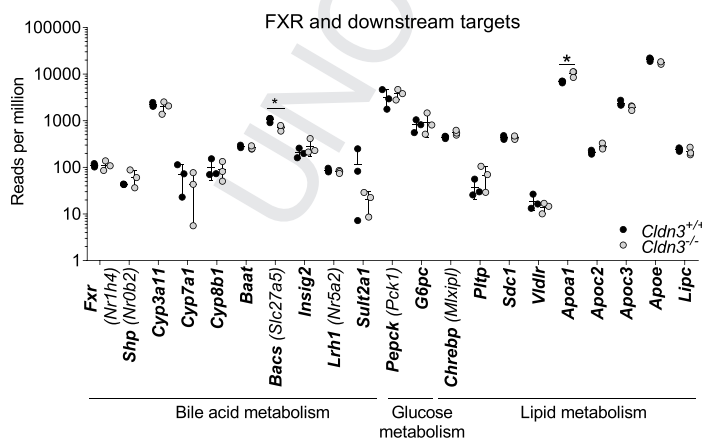
B



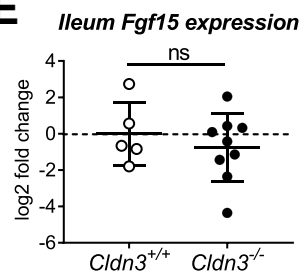
C



D



E



web 4C/FPO

1415 same animal housing facility. Mice were housed under
 1416 specific pathogen-free conditions at 22°C, 55% relative hu-
 1417 midity, with free access to chow and water, and in a 12-
 1418 hour, light-cycle controlled room. Green Line individually
 1419^{q19} vented cages (Tecniplast) were used at positive pressure.
 1420 Safe Aspen (S-Aspen-09322; JRS) cage bedding was used.
 1421 Animal cages contained enrichment and activation tools
 1422 such as plastic mouse house (Tecniplast), Nestlet or Sizzle
 1423 nests (Plexx), and Pura Crinkle Brown Kraft Paper (Labo-
 1424 dia). Mice were fed a standard dry pellet cereal-based diet
 1425 (10343200PXV20; Kliba Nafag). Interventions were per-
 1426 formed during the light phase in 12- to 18-week-old male
 1427 and female mice (weight, ~18–22 g). Liver regeneration
 1428 was studied using a standard model of PHx by removing the
 1429 left and medial liver lobes as previously described.⁶⁸ Mice
 1430 were killed by exsanguination under deep anesthesia. All
 1431 mouse experiments were performed with the approval of
 1432 the Veterinary Office of the Canton Bern (permit BE51/18),
 1433 according to the guidelines of good animal practice as
 1434 defined by the Office of Laboratory Animal Welfare, and
 1435^{q20} adhering to the standards of the nc3rs guidelines ([https://](https://www.nc3rs.org.uk/arrive-guidelines)
 1436 www.nc3rs.org.uk/arrive-guidelines).
 1437

1438 Single-Cell RNA Sequencing

1439^{q21} The unique molecular identified (UMI) matrix of our
 1440 recently published scRNA-seq was downloaded (GEO
 1441 accession number: GSE134134).²⁶ We removed cells with
 1442 more than 15% UMIs coming from mitochondrial genes and
 1443 cells with more than 25% UMIs coming from globin genes.
 1444 In addition, a cell containing an abnormally high number of
 1445^{q22} UMIs (110270) was excluded. Next, we removed genes that
 1446 were not expressing at least 2 reads in 2 genes. After data
 1447 preprocessing, the UMI matrix was processed as previously
 1448 described.²⁶ Shortly, we transformed the UMI matrix into a
 1449^{q23} Seurat object with Seurat 2 (PMID: 31178118). The data of
 1450 the Seurat object were log-normalized, the variable genes
 1451 were identified, and the data were scaled. Next, we
 1452^{q24} computed the principal component analysis with the R
 1453 function *RunPCA*, we identified the clusters with the R
 1454 function *FindClusters* with *dims.use=1* and *resolution=1*.
 1455 Finally, we computed the t-distributed stochastic neighbor
 1456 embedding coordinates with the R function *RunTSNE* with
 1457 *dims.use=1:8*.

1458 **Cell identification.** In Figure 1B, we show the expression
 1459 of the following cell population markers (Figure 1B shows
 1460^{q25} markers in bold font): hepatocytes: *Alb* (marker), *Apoa1*,
 1461 *G6pc*, *Hnf4a*, *Asgr1*, *Mup3*, *Pck1*; cholangiocytes: *Krt7*
 1462 (marker), *Krt19*, *Muc1*, *St14*; endothelial cells: *Pecam1*
 1463 (marker), *Dpp4*, *Oit3*, *Gpr182*, *Lyve1*, *Ushbp1*, *Tek*; stellate
 1464 cells: *Des* (marker), *Reln*, *Rbp1*, *Prnp*, *Vcl*, *Hhip*, *Col1A1*; and
 1465 immune cells: *Ptprc* (*Cd45*) (marker). Based on clustering
 1466

1474 and gene expression, we defined cluster 9 as hepatocytes;
 1475 cluster 7 as cholangiocytes; clusters 2, 4, 5, 8, 11, and 12 as
 1476 immune cells; clusters 0, 1, 3, 10, and 13 as endothelial cells;
 1477 and cluster 6 as stellate cells (Figure 1A).

1478 **Data visualization.** To display the gene expression, the
 1479 preprocessed UMI matrix was normalized with the function
 1480 *library.size.normalization* of the R package *Magic*.⁶⁹

1481 The dropout correction was performed with the R
 1482 function *magic* with parameters *genes="all_genes"*. The
 1483 dropout corrected data were displayed on the t-distributed
 1484 stochastic neighbor embedding plots.

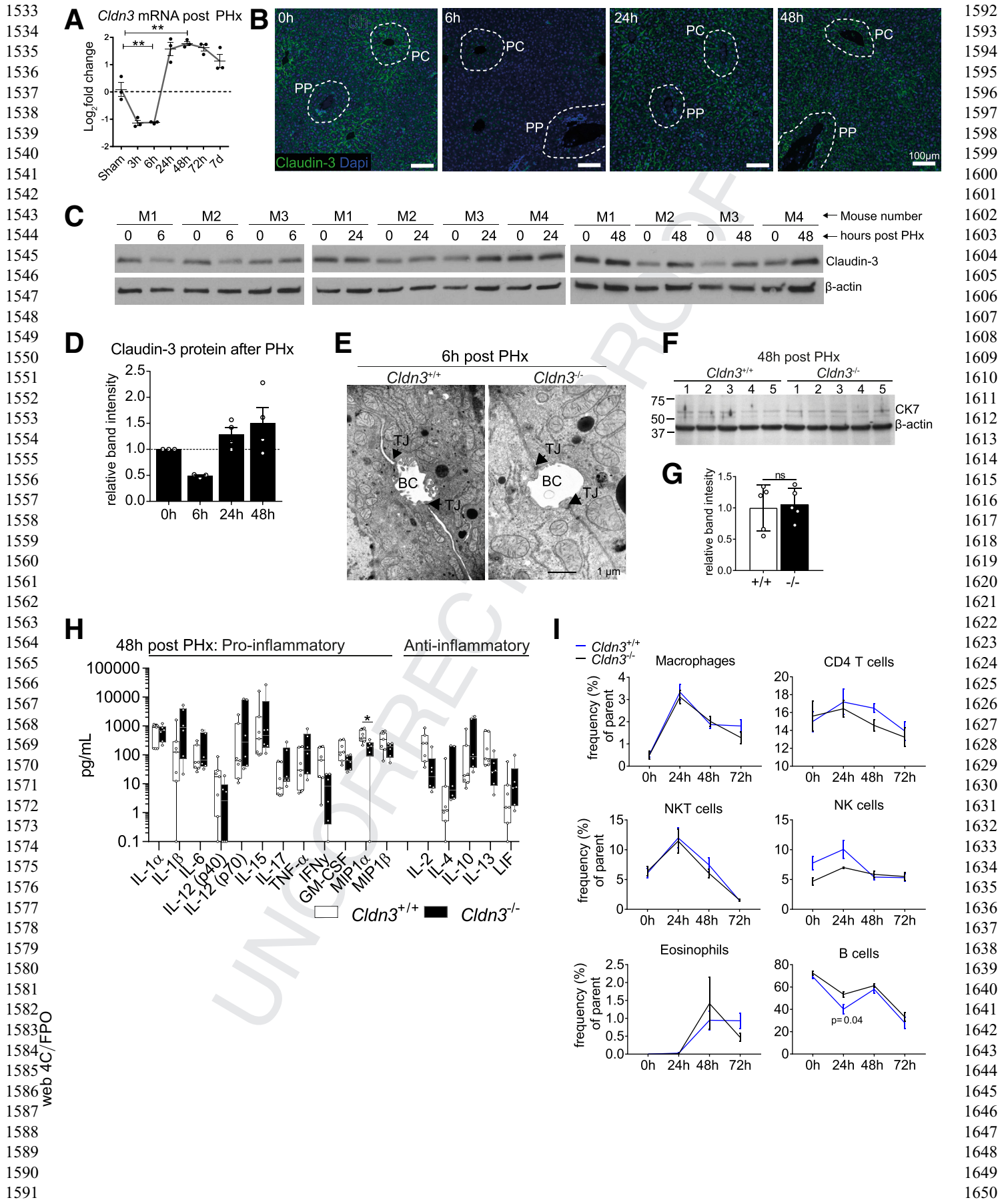
1485 **Heatmap.** The unsupervised clusters containing the same
 1486 cell types were merged and we averaged the UMI expres-
 1487 sion in each cell type, the average expression of each gene
 1488 was normalized from 0 to 1, $f(x) = (x - \min(x)) / (\max(x) - \min(x))$,
 1489 and represented as a heatmap with the R package
 1490 *gplots*.

1492 Histology

1493 **Immunohistochemistry and immunofluorescence.** Paraffin-embedded liver tissue was
 1494 sectioned at a thickness of 6 μm for conventional imaging or
 1495 30 μm for confocal z-stack imaging. Slides were deparaffin-
 1496 ized and hydrated in a xylol and ethanol series. For nuclear
 1497 staining, membrane permeabilization was performed by 20-
 1498 minute incubation in phosphate-buffered saline (PBS)-
 1499 Triton X-100 (0.4%) (1.09468.0100 and 108603; Merck,
 1500 Germany).

1502 Antigen retrieval was performed by heat-induced
 1503 epitope retrieval for 10 minutes at 95°C in citrate buffer,
 1504 pH 6.0 (C9999; Sigma-Aldrich). Nonspecific antibody bind-
 1505^{q27} ing was blocked at room temperature for 1 hour using a
 1506 protein-blocking solution (X0909; Dako). Antibodies were
 1507 prepared in antibody diluent (S3022; Dako) at the following
 1508 dilutions. Primary antibodies were as follows: Ki67 (RM-
 1509 9106-S1, 1:300; Thermo Fisher Scientific); anti-phospho-
 1510 histone H3 (06-570, 1:250; Merck Millipore); claudin-3
 1511 (NBP1-35668, 1:50; Novus Biologicals); and cytokeratin 7
 1512 (NBP1-88080, 1:200; Novus Biologicals). Secondary anti-
 1513 bodies were as follows: anti-rabbit-Cy5 (A10523, 1:300; Life
 1514 Sciences); anti-mouse Alexa 488 (A-11001, 1:300; Life Sci-
 1515 ences); and polyclonal rabbit anti-goat immunoglobulins/
 1516 horseradish peroxidase (P0449; Dako). For the development
 1517 of immunohistochemistry staining, streptavidin-peroxidase
 1518 (71-00-38; BioConcept) and 3,3'-diaminobenzidine tetra
 1519 hydrochloride (D4293-50SET; Sigma-Aldrich) were used.
 1520 Primary antibodies were incubated with gentle agitation
 1521 inside a wet chamber overnight at 4°C. Slides were washed
 1522 for 20 minutes in PBS-Tween-20 (0.5%, P1379; Sigma-
 1523 Aldrich) and incubated in darkness for 90 minutes with
 1524 the secondary antibodies and 4',6-diamidino-2-phenylindole
 1525

1526
 1527 **Figure 6. (See previous page). Loss of claudin-3 increases hepatic expression of the bile acid transporter *Ost1- β* .** (A)
 1528 Photographs of *Cldn3*^{+/+} and *Cldn3*^{-/-} gallbladders (n = 7). (B) RNA-seq data showing expression of bile transporters (n = 3,
 1529 means \pm SD, **P* < .05, unpaired *t* test). (C) Comparative real-time qPCR determining the transcriptional levels of hepatic *Ost1- β*
 1530 (*Slc51b*), *Asbt* (*Slc10a2*), and *Mdr3* (*Abcb4*) (n = 6, means \pm SD, **P* < .05, unpaired *t* test). (D) RNA-seq data showing hepatic
 1531 expression of *Fxr* and its downstream targets (n = 3, means \pm SD, **P* < .05, unpaired *t* test). (E) Comparative real-time qPCR
 1532 determining the transcriptional levels of *Fgf15* in the ileum (n = 5 for *Cldn3*^{+/+} and n = 9 for *Cldn3*^{-/-}, means \pm SD, unpaired *t*
 1533 test). FXR, farnesoid X-receptor; NE, not expressed.



1651 (DAPI) (D9542, diluted 1:2000; Sigma-Aldrich). After a final
1652 wash in PBS-Tween-20 (0.5%), slides were mounted with
1653 fluorescence mounting medium (H-1000; Vectorlabs) and
1654 the coverslip was fixed with nail polish. For immunohisto-
1655 chemistry staining, erythrocytes were lysed in 5% H₂O₂ for
1656 10 minutes before the first antibody incubation, and the
1657 staining was developed after the secondary antibody
1658 application by incubation with streptavidin-peroxidase for
1659 30 minutes and 3,3'-diaminobenzidine tetra hydrochloride
1660 for 1 minute. Representative images that were selected for
1661 display in the publication were moderately adjusted in
1662 brightness and color intensity with the help of image editing
1663 software. Importantly, adjustments were always made in
1664 the same way for all samples.

1665 For image acquisition, sections with 6- μ m or 10- μ m
1666 thickness were imaged using a fluorescent and bright-field
1667 microscope (panoramic 250 Flash III, 3DHISTECH, pano-
1668 ramic scanner software). Sections (30 μ m) were imaged
1669 with a confocal microscope (LSM 710; Zeiss), and 3-
1670 dimensional reconstructions from z-stack images were
1671 made using the Zeiss Zen software (Black edition, release
1672 version 8.1). Quantification of staining intensity and auto-
1673 mated counting of Ki67-/pHH3-positive nuclei was per-
1674 formed exclusively on unmodified raw images.

1675 **H&E staining.** Liver paraffin sections were stained with
1676 hematoxylin (HX43078349; Merck) for 6 minutes and
1677 differentiated in HCL-ALC (1:1) performing 3 dips. Slides
1678 were incubated in eosin (45240; Fluka Chemical Corp) for 3
1679 minutes, followed by dehydration and mounting with Eukitt
1680 (Kindler, Germany).

1681 Hepatic proliferation was quantified by imaging of 4
1682 randomly chosen regions per liver, containing approxi-
1683 mately 1000 DAPI-positive nuclei per region. Ki67- and
1684 pHH3-positive nuclei were counted and normalized as the
1685 percentage of all DAPI-positive cells with the help of ImageJ
1686 software (version 1.48; National Institutes of Health,
1687 Bethesda, MD).

1688 **Oil-red-O staining and quantification.** Liver tissue was
1689 embedded in Tissue-Tek O.C.T. medium (4583; Sakura
1690 Finetek, Germany), and 5- μ m cryosections were cut
1691 (CM3050S Cryostat; Leica). Slides subsequently were

1710 stained with Oil-Red-O (O0625; Sigma-Aldrich): frozen sec-
1711 tions were brought to room temperature, rinsed briefly in
1712 60% triethyl phosphate (538728; Sigma-Aldrich), and sub-
1713 sequently stained in 0.5% Oil-red-O for 20 minutes. After a
1714 wash in distilled water, sections were counterstained in
1715 filtered hematoxylin (HX43078349; Merck) for 90 seconds,
1716 and nuclei were blued in saturated lithium carbonate
1717 (1.05680.0250; VWR) for 15 seconds. Slides then were
1718 rinsed with a flow of water for 5 minutes and mounted with
1719 glycerin jelly.

1720 For staining quantification, a method based on pre-
1721 viously published quantification techniques was
1722 used.^{72,73} The image analyzing software Fiji was used.⁷⁴
1723 Magnified images (40 \times) with areas of the exact same
1724 sizes of 4 randomly chosen areas per sample were taken.
1725 Color deconvolution was performed (with the pre-set "H
1726 AEC") to separate the hematoxylin and the Oil-red-O
1727 staining. The lipid droplet contained in the red channel
1728 was selected, and the threshold was adjusted to the same
1729 level for each image (values, 0 and 200). The threshold-
1730 adjusted image then was converted to a black-and-
1731 white 8-bit image ("apply"). The intensity of the stain-
1732 ing then was measured with the analyze -> measure
1733 option. Staining intensities are given as integrated
1734 density.

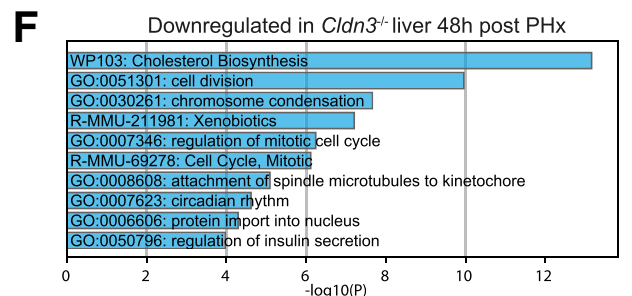
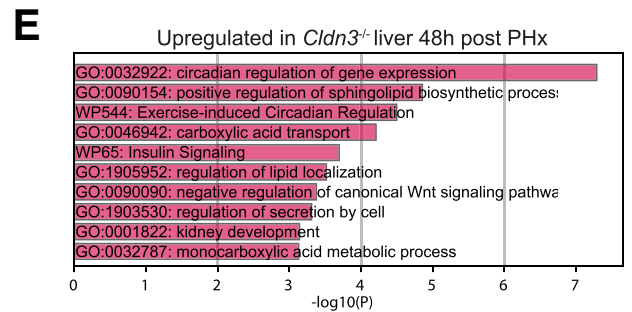
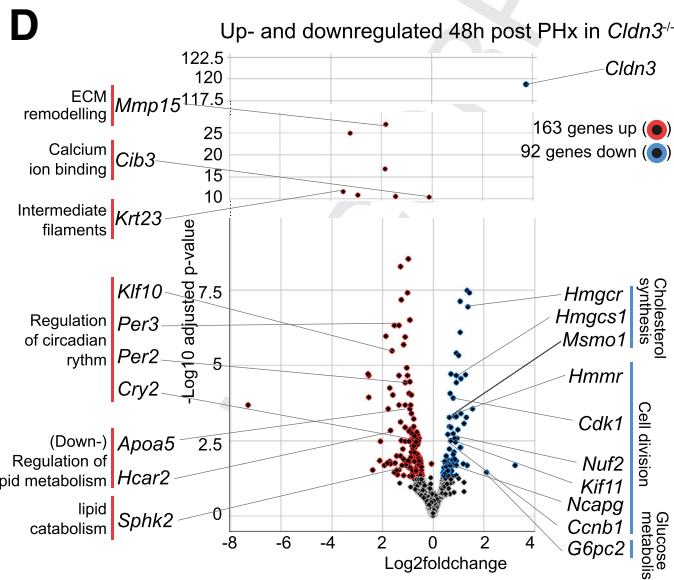
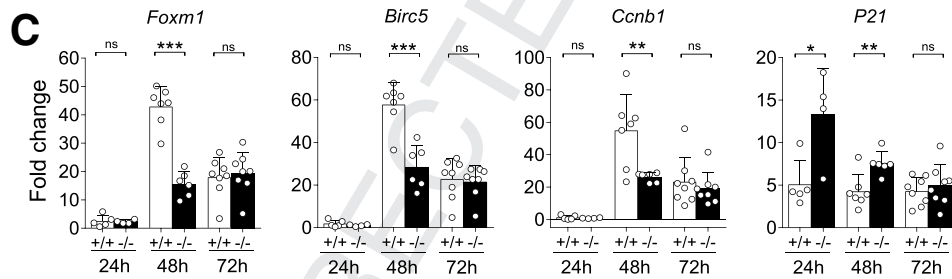
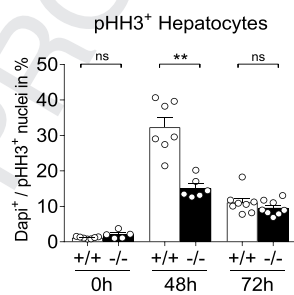
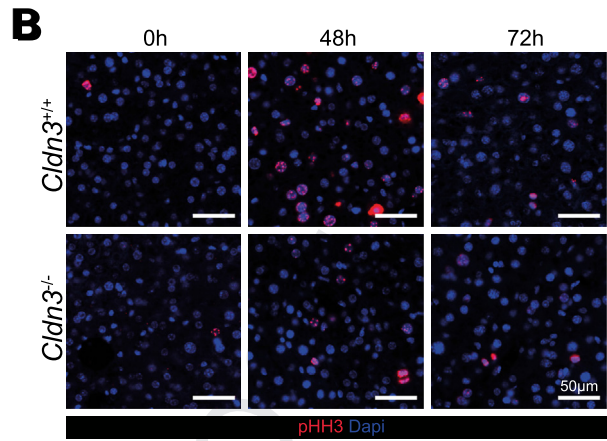
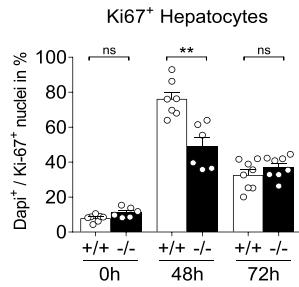
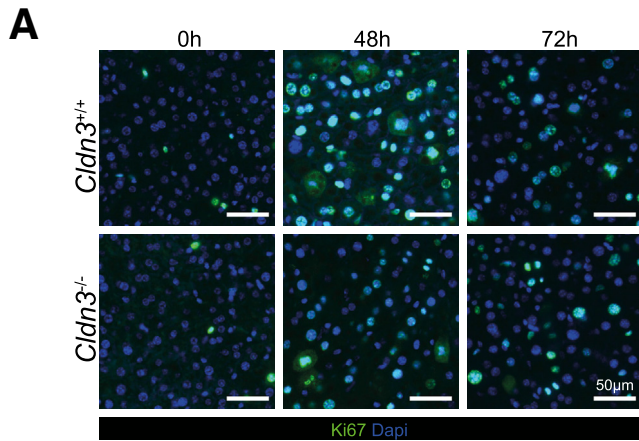
1735 **Masson trichrome staining.** Paraffin-embedded liver
1736 tissue was dewaxed and placed in Bouin's fixative (HT10-1-
1737 32; Sigma-Aldrich) at 56°C for 10 minutes. After washing
1738 slides in tap water and distilled H₂O, slides were stained
1739 with hematoxylin (HT10-79; Sigma-Aldrich) for 5 minutes.
1740 After washing in running tap water and distilled H₂O, slides
1741 were destained once with HCl-alcohol (1:1) and rinsed again
1742 in distilled H₂O. Next, slides were put in Biebrich scarlet-
1743 fuchsin (HT151-250ML; Sigma-Aldrich) diluted 1:2 in
1744 1% acetic acid (K45741563 425; Dr. Grogg Chemie) for 1
1745 minute. Slides were rinsed and stained with
1746 phosphomolybdic-phosphotungstic acid (HT153-250ML and
1747 HT152-250ML; Sigma) 1:1 for 5 minutes. Slides then were
1748 stained with Aniline Blue (HT154-250ML; Sigma) for 20
1749 minutes. After a last rinse, slides were put in 0.75% acetic
1750 acid, dehydrated, and mounted with Eukitt (Kindler).

1751
1752
1753
1754
1755
1756
1757
1758
1759
1760
1761
1762
1763
1764
1765
1766
1767
1768
1769
1770
1771
1772
1773
1774
1775
1776
1777
1778
1779
1780
1781
1782
1783
1784
1785
1786
1787
1788
1789
1790
1791
1792
1793
1794
1795
1796
1797
1798
1799
1800

Figure 7. (See previous page). *Cldn3* expression is regulated after PHx and claudin-3 loss does not induce inflammation in regenerating livers. Comparative real-time qPCR determining the transcriptional levels of *Cldn3* during a 7-day time course after PHx (n = 3, **P < .01, unpaired t test). (B) Anti-claudin-3 immunofluorescent stainings (green) in liver after PHx, and DAPI in blue. Representative images were taken. (C) Liver tissue Western blot for claudin-3 (20 kilodaltons) and β -actin (42 kilodaltons) at the indicated time points after PHx (n = 3/0–6 h, n = 4/0–24 h, n = 4/0–48 h). (D) Quantification of the Western blot in panel C. (E) Transmission electron microscopy images in liver tissue 6 hours after PHx. Arrowheads point to intact TJs located at *Cldn3*^{+/+} and *Cldn3*^{-/-} bile canaliculi (BC). (F and G) Quantification of ductular reaction in liver tissue. Total liver protein was isolated 48 hours after PHx and used for anti-CK7 Western blot. Band intensities were normalized to β -actin. Expression of hepatic CK7 was similar in *Cldn3*^{+/+} and *Cldn3*^{-/-} mice (n = 5, unpaired t test, *Cldn3*^{+/+} band intensities were compared with their group average). (H) Serum cytokine levels 48 hours after PHx. With the exception of a slightly decreased MIP1 α concentration in *Cldn3*^{-/-} mice, there were no significant differences comparing the groups (n = 7 for *Cldn3*^{+/+} and n = 6 for *Cldn3*^{-/-}, means \pm SEM, *P < .05, unpaired t test). (I) Fluorescence-activated cell sorting analysis of hepatic immune cell frequencies at the indicated times after PHx. Despite a slightly higher B-cell frequency at 24 hours in *Cldn3*^{-/-} mice, there were no significant differences compared with *Cldn3*^{+/+} mice (at 0 h and 24 h: n = 5 for *Cldn3*^{+/+} and n = 4 for *Cldn3*^{-/-}; 48 h, n = 5; 72 h, n = 8; unpaired t test). Microscopes used for image acquisition in this figure were as follows: immune fluorescence, panoramic 250 Flash III, 3DHISTECH, panoramic scanner software, with a 20 \times objective; electron microscopy, Philips CM 12. CK7, _____; GM-CSF, _____; IFN γ , interferon γ ; IL, interleukin; LIF, _____; MIP1 α , _____; NK, _____; NKT, _____; PC, peri-central; PP, periportal; TNF- α , tumor necrosis factor α .

1769
1770
1771
1772
1773
1774
1775
1776
1777
1778
1779
1780
1781
1782
1783
1784
1785
1786
1787
1788
1789
1790
1791
1792
1793
1794
1795
1796
1797
1798
1799
1800
1801
1802
1803
1804
1805
1806
1807
1808
1809
1810
1811
1812
1813
1814
1815
1816
1817
1818
1819
1820
1821
1822
1823
1824
1825
1826
1827

1828
1829
1830
1831
1832
1833
1834
1835
1836
1837
1838
1839
1840
1841
1842
1843
1844
1845
1846
1847
1848
1849
1850
1851
1852
1853
1854
1855
1856
1857
1858
1859
1860
1861
1862
1863
1864
1865
1866
1867
1868
1869
1870
1871
1872
1873
1874
1875
1876
1877
1878
1879
1880
1881
1882
1883
1884
1885
1886



1887 Measurement of ALT, AST, and ALP in Serum

1888 The liver injury markers ALT and AST were measured on
1889 the Cobas 8000 modular analyzer using the module C502
1890 (Roche, Switzerland). ALP likewise was measured on the
1891 Cobas 8000, using the module C702 (Roche, Switzerland).
1892 All measurements were performed following the manufac-
1893 turer's instructions.

1894

1895

1896 Electron Microscopy

1897 Sample preparation and electron microscopy were per-
1898 formed as published previously.⁷⁵ A variance in the cited
1899 protocol was used. In the lanthanide fixation step, samples
1900 were incubated in a water bath for 15 minutes at 50°C,
1901 without a prior incubation at room temperature. Trans-
1902 mission electron microscopy images were acquired using a
1903 Philips CM 12 microscope (Philips/Fei, The Netherlands).

1904

1905

1906 Flow Cytometry

1907 Antibodies used for fluorescence-activated cell sorting
1908 can be found in Table 1. Livers were perfused with PBS via
1909 the portal vein until blanched and then put in Iscove's
1910 modified Dulbecco's medium (Gibco), supplemented with
1911 10% fetal bovine serum. Whole livers were passed through
1912 a metal spleen screen and digested with 0.05% collagenase
1913 IV (Worthington Biochemical) and DNase I (Sigma-Aldrich)
1914 for 30 minutes at 37°C. Intrahepatic mononuclear cells were
1915 purified on a Percoll gradient after centrifugation at 1250 ×
1916 g for 20 minutes without braking. Cells subsequently were
1917 washed twice with PBS, and then resuspended in PBS con-
1918 taining 3% fetal bovine serum. Aliquots of 10⁶ cells/100 μL
1919 of staining buffer per well were incubated each with 1 μg of
1920 purified anti-CD16/CD32 for 20 minutes in the dark to
1921 block nonspecific binding of antibodies to the FcγIII and
1922 FcγII receptors. Cell suspensions were incubated with cell
1923 viability dye eFluor 506 (Thermo Fisher Scientific) for 20
1924 minutes at 4°C in the dark to exclude dead cells. Subse-
1925 quently, these cells were stained separately with the
1926 following surface markers for 15 minutes with 1 μg of pri-
1927 mary antibodies (Table 1). For cytokines and transcription
1928 factors, cells first were stained with antibodies to surface
1929 antigens, subsequently fixed, and permeabilized according
1930 to the manufacturer's instructions (Foxp3/Transcription
1931 Factor Staining Buffer Set; eBioscience). Corresponding
1932 fluorochrome-labeled isotype control antibodies were used
1933 for staining controls. Cells resuspended in 250 μL of buffer

1934

1935

1936

1937

1938

1939

1940

1941

1942

1943

1944

1945

1946

1947

1948

1949

1950

1951

(0.15 mol/L NaCl, 1 mmol/L NaH₂PO₄ H₂O, 10 mmol/L
Na₂HPO₄ 2H₂O, and 3 mmol/L NaN₃) were analyzed in a
flow cytometer (BD LSR II; BD Pharmingen, Inc, San Diego,
CA) using the corresponding BD FACSDiva software. Flow
cytometric analysis was performed using FlowJo software
(Treestar, Inc, Ashland, OR).

Western Blot

Total protein was extracted from liver tissue or cultured
cells using RIPA lysis buffer and a TissueLyser II (Qiagen).
Lysates were centrifuged for 15 minutes at 20,000 × g, and
the supernatant was aliquoted. Protein concentrations were
quantified by Bradford assay (5000006; Bio-Rad) and a
microplate reader. Precast gels (456-1094; Bio-Rad) were
used to separate equalized amounts of protein per sample
by sodium dodecyl sulfate-polyacrylamide gel electropho-
resis, under reducing conditions. Proteins then were trans-
ferred on nitrocellulose membranes (170-4158; Bio-Rad).
Membranes were blocked with 5% w/v nonfat dry milk in
PBS for 1 hour at room temperature. Primary antibodies
were diluted in the blocking medium and incubated over-
night at 4°C. Primary antibodies were as follows: claudin-3
(NBP1-35668, 1:500–1:1000; Novus Biologicals); cytoker-
atin 7 (NBP1-88080, 1:200; Novus Biologicals); and anti-β-
actin- peroxidase (A3854, 1:50,000; Sigma-Aldrich); the
secondary antibody used was anti-rabbit-horseradish
peroxidase (P0448, 1:2000; Dako).

After primary antibody incubation, membranes were
washed 3 times for 5 minutes in PBS-Tween-20 (0.1%).
Secondary antibodies were diluted with 5% w/v nonfat dry
milk in PBS, and the membranes were incubated for 1 hour
at room temperature, followed by 3 washing steps for 30
minutes in total. Enhanced chemiluminescence solution
(NEL105001EA; Perkin Elmer) was added for 1 minute to
develop the signal. Films in combination with a developer
(AGFA, CURIX 60) were used to visualize the bands. The
correct band size was estimated with the help of a standard
protein ladder (161-0374; Bio-Rad).

Real-Time qPCR mRNA Expression Analysis

RNA from snap-frozen tissue has been extracted using
NucleoZOL (740404.200; Macherey-Nagel). Complementary
DNA was made from 500 ng of tissue RNA using the
OmniScript reverse-transcriptase kit (205113; Qiagen). Per
reaction, 11.25 ng complementary DNA was used. Real-time

Figure 8. (See previous page). Claudin-3 contributes to optimal liver regeneration. (A and B) Immunofluorescent staining of anti-Ki67 (green) or anti-pHH3 (red) in liver tissue after PHx, comparing *Cldn3*^{+/+} and *Cldn3*^{-/-} livers. DAPI in blue. Quantification of the proliferation scores below (0 h and 48 h: n = 7 for *Cldn3*^{+/+} and n = 6 for *Cldn3*^{-/-}; 72 h: n = 8, bars represent the means ± SEM, **P < .01, unpaired t test). Representative images were taken. (C) Comparative real-time qPCR determining the cell-cycle-related gene expression after PHx (24 h: n = 5 for *Cldn3*^{+/+} and n = 4 for *Cldn3*^{-/-}; 48 h: n = 7 for *Cldn3*^{+/+} and n = 6 for *Cldn3*^{-/-}; 72 h: n = 8, bars represent means ± SEM, *P < .05, **P < .01, ***P < .001, unpaired t test). (D) Volcano plot showing up-regulated and down-regulated genes (red circles and blue circles, respectively) in *Cldn3*^{-/-} compared with *Cldn3*^{+/+} liver tissue at 48 hours after PHx. RNA-seq analysis is performed by DESeq2 (n = 3, differential expression significance threshold: P value adjusted < .05). Genes with low expression in *Cldn3*^{-/-} are shown in blue, and with high expression in red circles. Genes with high significance and genes part in the regulated pathways are annotated. Metascape analysis of the (E) top 10 up-regulated and (F) top 10 down-regulated gene pathways within the data set of panel D. Microscopes used for image acquisition in this figure were as follows: panoramic 250 Flash III, 3DHISTECH, panoramic scanner software, with a 20× objective. ECM, _____.

Table 1. Antibodies Used for Fluorescence-Activated Cell Sorting

Fluorescence	Cell marker	Clone	Company	Catalog no.
Alexa Fluor 700	NK1.1	PK136	BioLegend	108730
PE-cy5	NK1.1	PK136	BioLegend	108716
PE-eFluor-610	Eomes	Dan11mag	eBioscience	61-4875-82
APC	Roryt	AFKJS-9	eBioscience	17-6988-80
APC-eFluor780	PD-1	J43	eBioscience	47-9985-82
eFluor450	PD-1	J43	eBioscience	48-9985-82
PE	IL-22	Poly5164	BioLegend	516404
Percp-eFluor710	IL-22	1H8PWSR	eBioscience	46-7221-80
PE-cy7	CD49b	DX5	BioLegend	108922
PE-cy7	CD4	GK1.5	eBioscience	25-0041-81
APC	CD4	RM4-4	BioLegend	116014
BV570	CD8	53-6.7	BioLegend	301038
Alexa Fluor 700	CD11b	M1/70	BioLegend	101222
BV421	CD49a	Ha31/8	BD Biosciences	740046
APC-eFluor780	INF- γ	XMG1.2	eBioscience	47-7311-82
FITC	INF- γ	XMG1.2	BioLegend	505806
PE	INF- γ	XMG1.2	eBioscience	12-7311-41
PE	CD19	SJ25C1	eBioscience	12-0198-41
PE-Dazzle 594	CD19	6D5	BioLegend	115554
BUV395	CD45	30-F11(Ruo)	BD Biosciences	564279
Percp cy.5.5	FoxP3	FJK-16s	eBioscience	45-5773-80
PE	FoxP3	FJK-16s	eBioscience	12-5773-80
PE-Dazzle 594	CD152	UC10-4B9	BioLegend	106318
APC	IL-10	JES5-16E3	BioLegend	505010
PE	IL-10	JES3-9D7	eBioscience	12-7108-41
FITC	CD69	H1.2F3	BioLegend	104506
PE	Ly6G	RB6-8C5	eBioscience	12-8931-81
PE-cy7	Ly6G	RB6-8C5	eBioscience	25-5931-81
APC	F4/80	BM8	eBioscience	17-4801-82
eFluor450	CD11c	N418	eBioscience	48-0114-82
FITC	TNF α	MP6-XT22	BioLegend	506304
eFluor506	Viability dye	-	eBioscience	65-0866-18
-	CD16/CD32	2.4 G2	BioLegend	101302

qPCRs have been performed on an ABI 7500 thermocycler (Applied Biosystems) using TaqMan and on an ABI 7900 HT thermocycler (Applied Biosystems) for the SYBR green-based assays. The corresponding reaction mixtures (TaqMan, 4914058001 and SYBR green, 000000004913914001; both Sigma-Aldrich) were used. Cycling conditions were chosen according to the vendor instructions of the DNA polymerase master mixes. TaqMan real-time qPCR primers used were as follows: *Ccnb1* (Mm03053893_gH; Thermo Fisher Scientific), *Birc5* (Mm00599749_m1; Thermo Fisher Scientific), *Foxm1* (Mm00514924_m1; Thermo Fisher Scientific), *Cdkn1a* (p21) (Mm00432448_m1; Thermo Fisher Scientific), *Tbp* (Mm00446971-m1; Thermo Fisher Scientific), *Mdr3* (4448892; Thermo Fisher Scientific), *Ost1- β* (Mm01175040_m1; Thermo Fisher Scientific), and *Asbt* (Mm00488258_m1; Thermo Fisher Scientific). SYBR real-

time qPCR primers used were as follows: *Cldn3* forward: GCACCCACCAAGATCCTCTA, *Cldn3* reverse: TCGTCTGTCAC-CATCTGGAA (*Cldn3* SYBR primer has been published⁷⁶), *Fgf15* forward: CCAACTGCTTCCTCCGAATCC, *Fgf15* reverse: TACAGTCTTCCTCCGAGTAGC, *Eef1a1* forward: CGTTCTTTTTCGCAACGGGT, *Eef1a1* reverse: TTGCCGGAATCTACGTGTCC (designed with NCBI Primer-BLAST). Fold- and log₂-fold changes in gene expression were calculated using the $\Delta\Delta$ CT method.

RNA Sequencing

Total RNA was extracted from the liver with NucleoZOL (740404.200; Macherey-Nagel), and quantified by a bio-analyzer (Bio-Rad). Sequencing was prepared with paired-end reads of 50 bp, TruSeq Stranded mRNA (Illumina). Sequencing was performed on a NovaSeq6000 (Illumina).

2123 **RNA-seq alignment.** Fastq files were aligned to the
2124 mouse reference genome mm10 ENSEMBL release 102⁷⁷
2125 with hisat2 v. 2.2.1,⁷⁸ and transformed into bam files with
2126 SAMtools v. 1.10.⁷⁹ The read count matrix was produced
2127 from the bam files via featureCount shell version 2.0.1.⁸⁰

2128 **Dimensionality reduction.** For the principal component
2129 analysis, the read count matrix was variance-stabilizing--
2130 transformed using vst(), then principal components were
2131 computed and visualized using plotPCA() functions from the
2132 DESeq2 R package,⁷⁹ with default parameters.

2133 **RNA-seq differential expression.** Differentially
2134 expressed genes were computed with R package DESeq2.
2135 Two technical replicates of control sample 5 were analyzed
2136 together by collapsing them using the DESeq2 *collapseR-*
2137 *replicates* function. Genes with a *P* value less than .05
2138 adjusted by false discovery rate were considered statisti-
2139 cally significant for further analysis. For volcano plot visu-
2140 alization, log₂-fold changes obtained from DESeq2 analysis
2141 were shrunk using the apeglm shrinkage estimator.⁸²

2142 **Enrichment analysis.** Metascape⁸¹ was used to deter-
2143 mine the pathways to which genes were associated.

2145 Oral Glucose Tolerance Test, Glucose, and 2146 Insulin Measurements

2147 Before the oral glucose tolerance test, mice were fasted
2148 overnight (16 hours), followed by baseline blood glucose
2149 and insulin levels measurements. A bodyweight-adjusted
2150 amount of glucose was given by oral gavage (2 mg/g
2151 bodyweight). Glucose and insulin levels subsequently were
2152 determined. Blood for glucose was obtained by blood
2153 collection from the left and right saphenous vein (<1 μL).
2154 Blood/serum for insulin measurements was obtained by
2155 exsanguination (under anesthesia) via cardiac puncture.
2156 Glucose levels were determined with the use of a com-
2157 mercial glucometer (Accu-chek Aviva; Roche, Switzerland).
2158 Serum insulin levels were determined with the Ultra-
2159 Sensitive Mouse Insulin ELISA Kit (90080; Crystal Chem),
2160 according to the manufacturer's instructions.

2163 Bile Acid Quantification

2164 The method applied was described recently.⁸² Briefly,
2165 for quantification of bile acids, 25-μL serum samples diluted
2166 1:4 with water, and calibrators, were subjected to protein
2167 precipitation by adding 900 μL of 2-propanol and a mixture
2168 of deuterated internal standards. Extraction was performed
2169 for 30 minutes at 4°C with continuous shaking, followed by
2170 centrifuging at 16,000 × g for 10 minutes. Supernatants
2171 were transferred to new tubes, evaporated to dryness, and
2172 reconstituted with 100 μL methanol:water (1:1, v/v). For
2173 the extraction of liver samples, 900 μL of chloro-
2174 form:methanol:water (1:3:1, v/v/v) and 100 μL internal
2175 standard mixture were added to a Precellys tube containing
2176 beads and 30 ± 5 mg of liver tissue. Samples were ho-
2177 mogenized with a Precellys tissue homogenizer, and
2178 centrifuged at 16,000 × g for 10 minutes at 20°C. The su-
2179 pernatant was transferred to a new tube and the procedure
2180 was repeated by adding 800 μL extraction solvent. After
2181 evaporation to dryness, samples were resuspended with

2182 200 μL methanol:water (1:1, v/v). The injection volume in
2183 both cases was 3 μL. Liquid chromatography-tandem mass
2184 spectrometry consisted of an Agilent 1290 UPLC coupled to
2185 an Agilent 6490 triple quadrupole mass spectrometer
2186 equipped with an electrospray ionization source (Agilent
2187 Technologies, Basel, Switzerland). Chromatographic sepa-
2188 ration of bile acids was achieved using a reversed-phase
2189 column (Acquity UPLC BEH C18, 1.7 mm, 2.1 μm, 150
2190 mm; Waters, Wexford, Ireland).⁸⁴

2192 Measurement of Serum Proinflammatory 2193 Cytokines

2194 Serum cytokines were determined on a Millipore Milli-
2195 plex (Merck) based cytokine array. The array was per-
2196 formed by Eve technologies (Calgary, Canada), using the
2197 following application: Chemokine Array 31-Plex (MD31).
2198

2200 Statistical Tests Used to Analyze Data

2201 The statistical tests used to analyze the data are fitted for
2202 each experiment and are described within each figure
2203 legend.

2204 All authors had access to the study data and have
2205 reviewed and approved the final manuscript.

2207 References

- 2208 1. Zihni C, Mills C, Matter K, Balda MS. Tight junctions:
2209 from simple barriers to multifunctional molecular gates.
2210 *Nat Rev Mol Cell Biol* 2016;17:564–580.
- 2211 2. Hwang I, Yang H, Kang H-S, Ahn C-H, Lee G-S, Hong E-
2212 J, An B-S, Jeung E-B. Spatial expression of claudin
2213 family members in various organs of mice. *Mol Med Rep*
2214 2014;9:1806–1812.
- 2215 3. Hwang I, An BS, Yang H, Kang HS, Jung EM, Jeung EB.
2216 Tissue-specific expression of occludin, zona occludens-
2217 1, and junction adhesion molecule A in the duodenum,
2218 ileum, colon, kidney, liver, lung, brain, and skeletal
2219 muscle of C57BL mice. *J Physiol Pharmacol* 2013;
2220 64:11–18.
- 2221 4. Pradhan-Sundd T, Monga SP. Blood-bile barrier:
2222 morphology, regulation, and pathophysiology. *Gene*
2223 *Expression* 2019;19:69–87.
- 2224 5. Ding L, Lu Z, Lu Q, Chen Y-H. The claudin family of
2225 proteins in human malignancy: a clinical perspective.
2226 *Cancer Manag Res* 2013;5:367–375.
- 2227 6. Günzel D, Yu ASL. Claudins and the modulation of tight
2228 junction permeability. *Physiol Rev* 2013;93:525–569.
- 2229 7. Colegio OR, Van Itallie CM, McCrean HJ, Rahner C,
2230 Anderson JM. Claudins create charge-selective channels
2231 in the paracellular pathway between epithelial cells. *Am J*
2232 *Physiol Cell Physiol* 2002;283:C142–C147.
- 2233 8. Tabariès S, Siegel PM. The role of claudins in cancer
2234 metastasis. *Oncogene* 2017;36:1176–1190.
- 2235 9. Lal-Nag M, Morin PJ. The claudins. *Genome Biol* 2009;
2236 10:235.
- 2237 10. Evans MJ, von Hahn T, Tscherne DM, Syder AJ, Panis M,
2238 Wölk B, Hatzioannou T, McKeating JA, Bieniasz PD,
2239 Rice CM. Claudin-1 is a hepatitis C virus co-receptor
2240

- required for a late step in entry. *Nature* 2007; 446:801–805.
- 2241
2242
- 2243 11. Benedicto I, Molina-Jimenez F, Bartosch B, Cosset F-L,
2244 Lavillette D, Prieto J, Moreno-Otero R, Valenzuela-
2245 Fernandez A, Aldabe R, Lopez-Cabrera M, Majano PL.
2246 The tight junction-associated protein occludin is required
2247 for a postbinding step in hepatitis C virus entry and
2248 infection. *J Virol* 2009;83:8012–8020.
- 2249 12. Meertens L, Bertaux C, Cukierman L, Cormier E,
2250 Lavillette D, Cosset F-L, Dragic T. The tight junction
2251 proteins claudin-1, -6, and -9 are entry cofactors for
2252 hepatitis C virus. *J Virol* 2008;82:3555–3560.
- 2253 13. Fujita K, Katahira J, Horiguchi Y, Sonoda N, Furuse M,
2254 Tsukita S. Clostridium perfringens enterotoxin binds to
2255 the second extracellular loop of claudin-3, a tight junc-
2256 tion integral membrane protein. *FEBS Lett* 2000;
2257 476:258–261.
- 2258 14. Roehlen N, Roca Suarez AA, El Saghire H, Saviano A,
2259 Schuster C, Lupberger J, Baumert TF. Tight junction
2260 proteins and the biology of hepatobiliary disease. *Int J*
2261 *Mol Sci* 2020;21:825.
- 2262 15. Tanaka H, Yamamoto Y, Kashihara H, Yamazaki Y,
2263 Tani K, Fujiyoshi Y, Mineta K, Takeuchi K, Tamura A,
2264 Tsukita S. Claudin-21 has a paracellular channel role at
2265 tight junctions. *Mol Cell Biol* 2016;36:954–964.
- 2266 16. Hadj-Rabia S, Baala L, Vabres P, Hamel-Teillac D,
2267 Jacquemin E, Fabre M, Lyonnet S, de Prost Y,
2268 Munnich A, Hadchouel M, Smahi A. Claudin-1 gene
2269 mutations in neonatal sclerosing cholangitis associated
2270 with ichthyosis: a tight junction disease. *Gastroenter-
2271 ology* 2004;127:1386–1390.
- 2272 17. Baala L, Hadj-Rabia S, Hamel-Teillac D, Hadchouel M,
2273 Prost C, Leal SM, Jacquemin E, Sefiani A, de Prost Y,
2274 Courtois G, Munnich A, Lyonnet S, Vabres P. Homozy-
2275 gosity mapping of a locus for a novel syndromic ich-
2276 thyosis to chromosome 3q27–q28. *J Invest Dermatol*
2277 2002;119:70–76.
- 2278 18. Matsumoto K, Yamazaki Y, Tanaka H, Watanabe M,
2279 Eguchi H, Nagano H, Hikita H, Tatsumi T, Takehara T,
2280 Tamura A, Tsukita S. Claudin 2 deficiency reduces bile
2281 flow and increases susceptibility to cholesterol gallstone
2282 disease in mice. *Gastroenterology* 2014;147:1134–1145.
e10.
- 2283 19. Bouchagier KA, Assimakopoulos SF, Karavias DD,
2284 Maroulis I, Tzelepi V, Kalofonos H, Karavias DD,
2285 Kardamakis D, Scopa CD, Tsamandas AC. Expression of
2286 claudins-1, -4, -5, -7 and occludin in hepatocellular
2287 carcinoma and their relation with classic clinicopatho-
2288 logical features and patients' survival. *In Vivo* 2014;
2289 28:315–326.
- 2290 20. Milatz S, Krug SM, Rosenthal R, Günzel D, Müller D,
2291 Schulzke J-D, Amasheh S, Fromm M. Claudin-3 acts as
2292 a sealing component of the tight junction for ions of
2293 either charge and uncharged solutes. *Biochim Biophys*
2294 *Acta* 2010;1798:2048–2057.
- 2295 21. Rahner C, Mitic LL, Anderson JM. Heterogeneity in
2296 expression and subcellular localization of claudins 2, 3,
2297 4, and 5 in the rat liver, pancreas, and gut. *Gastroen-
2298 terology* 2001;120:411–422.
- 2299 22. Tanaka H, Imasato M, Yamazaki Y, Matsumoto K,
Kunimoto K, Delpierre J, Meyer K, Zerial M, Kitamura N,
Watanabe M, Tamura A, Tsukita S. Claudin-3 regulates
bile canalicular paracellular barrier and cholesterol gall-
stone core formation in mice. *J Hepatol* 2018;
69:1308–1316.
- 2300 23. Garcia-Hernandez V, Quiros M, Nusrat A. Intestinal
2301 epithelial claudins: expression and regulation in homeo-
2302 stasis and inflammation: intestinal epithelial claudins.
2303 *Ann N Y Acad Sci* 2017;1397:66–79.
- 2304 24. Ahmad R, Rah B, Bastola D, Dhawan P, Singh AB.
2305 Obesity-induces organ and tissue specific tight junction
2306 restructuring and barrier deregulation by claudin
2307 switching. *Sci Rep* 2017;7:5125.
- 2308 25. Patel RM, Myers LS, Kurundkar AR, Maheshwari A,
2309 Nusrat A, Lin PW. Probiotic bacteria induce maturation of
2310 intestinal claudin 3 expression and barrier function. *Am J*
2311 *Pathol* 2012;180:626–635.
- 2312 26. Sanchez-Taltavull D, Perkins TJ, Dommann N, Melin N,
2313 Keogh A, Candinas D, Stroka D, Beldi G. Bayesian cor-
2314 relation is a robust gene similarity measure for single-cell
2315 RNA-seq data. *NAR Genom Bioinform* 2020;2:lqaa002.
- 2316 27. Castro Dias M, Coisne C, Lazarevic I, Baden P, Hata M,
2317 Iwamoto N, Francisco DMF, Vanlandewijck M, He L,
2318 Baier FA, Stroka D, Bruggmann R, Lyck R, Enzmann G,
2319 Deutsch U, Betsholtz C, Furuse M, Tsukita S,
2320 Engelhardt B. Claudin-3-deficient C57BL/6J mice
2321 display intact brain barriers. *Sci Rep* 2019;9:203.
- 2322 28. Fickert P, Wagner M. Biliary bile acids in hepatobiliary
2323 injury – what is the link? *J Hepatol* 2017;67:619–631.
- 2324 29. Woo S-L, Guo T, Wu C. Hepatic lipogenesis: nutritional
2325 control and pathophysiological relevance. In: Ntambi JM,
2326 ed. *Hepatic de novo lipogenesis and regulation of*
2327 *metabolism*. Cham: Springer International Publishing,
2328 2016:211–234.
- 2329 30. Ogrodnik M, Miwa S, Tchkonja T, Tiniakos D, Wilson CL,
2330 Lahat A, Day CP, Burt A, Palmer A, Anstee QM,
2331 Grellscheid SN, Hoeijmakers JHJ, Barnhoorn S,
2332 Mann DA, Bird TG, Vermeij WP, Kirkland JL, Passos JF,
2333 von Zglinicki T, Jurk D. Cellular senescence drives age-
2334 dependent hepatic steatosis. *Nat Commun* 2017;
2335 8:15691.
- 2336 31. Luo D, Li J, Chen K, Yin Y, Fang Z, Pang H, Rong X,
2337 Guo J. Study on metabolic trajectory of liver aging and
2338 the effect of Fufang Zhenzhu Tiaozhi on aging mice.
2339 *Front Pharmacol* 2019;10:926.
- 2340 32. Hunt NJ, Kang SW, Lockwood GP, Le Couteur DG,
2341 Cogger VC. Hallmarks of aging in the liver. *Comput*
2342 *Struct Biotechnol J* 2019;17:1151–1161.
- 2343 33. Fiorucci S, Biagioli M, Zampella A, Distrutti E. Bile acids
2344 activated receptors regulate innate immunity. *Front*
2345 *Immunol* 2018;9:1853.
- 2346 34. Sato Y, Koyama S, Tsukada K, Hatakeyama K. Acute
2347 portal hypertension reflecting shear stress as a trigger of
2348 liver regeneration following partial hepatectomy. *Surg*
2349 *Today* 1997;27:518–526.
- 2350 35. Takakuwa Y, Kokai Y, Sasaki K, Chiba H, Tobioka H,
2351 Mori M, Sawada N. Bile canalicular barrier function and
2352 expression of tight-junctional molecules in rat
2353 2354
2355
2356
2357
2358

- 2359 hepatocytes during common bile duct ligation. *Cell Tissue Res* 2002;307:181–189. 2418
- 2360 36. Kojima T. Tight junction proteins and signal transduction pathways in hepatocytes. *Histol Histopathol* 2009; 2419
- 2362 11:1463–1472. 2420
- 2363 37. Sakaguchi T, Suzuki S, Higashi H, Inaba K, Nakamura S, 2421
- 2364 Baba S, Kato T, Konno H. Expression of tight junction 2422
- 2365 protein claudin-5 in tumor vessels and sinusoidal endo- 2423
- 2366 thelium in patients with hepatocellular carcinoma. *J Surg 2424*
- 2367 Res 2008;147:123–131. 2425
- 2368 38. D'Agnillo F, Williams MC, Moayeri M, Warfel JM. Anthrax 2426
- 2369 lethal toxin downregulates claudin-5 expression in human 2427
- 2370 endothelial tight junctions. *PLoS One* 2013;8:e62576. 2428
- 2371 39. Holczbauer Á, Gyöngyösi B, Lotz G, Törzsök P, Kaposi- 2429
- 2372 Novák P, Szijártó A, Tátrai P, Kupcsulik P, Schaff Z, 2430
- 2373 Kiss A. Increased expression of claudin-1 and claudin-7 2431
- 2374 in liver cirrhosis and hepatocellular carcinoma. *Pathol 2432*
- 2375 Oncol Res 2014;20:493–502. 2433
- 2376 40. Inai T, Sengoku A, Guan X, Hirose E, Iida H, Shibata Y. 2434
- 2377 Heterogeneity in expression and subcellular localization 2435
- 2378 of tight junction proteins, claudin-10 and -15, examined 2436
- 2379 by RT-PCR and immunofluorescence microscopy. *Arch 2437*
- 2380 Histol Cytol 2005;68:349–360. 2438
- 2381 41. Morita K, Furuse M, Fujimoto K, Tsukita S. Claudin 2439
- 2382 multigene family encoding four-transmembrane domain 2440
- 2383 protein components of tight junction strands. *Proc Natl 2441*
- 2384 Acad Sci U S A 1999;96:511–516. 2442
- 2385 42. D'Souza T, Sherman-Baust CA, Poosala S, Mullin JM, 2443
- 2386 Morin PJ. Age-related changes of claudin expression in 2444
- 2387 mouse liver, kidney, and pancreas. *J Gerontology A Biol 2445*
- 2388 Sci Med Sci 2009;64A:1146–1153. 2446
- 2389 43. Gebhardt R, Matz-Soja M. Liver zonation: novel aspects 2447
- 2390 of its regulation and its impact on homeostasis. *World J 2448*
- 2391 Gastroenterol 2014;20:8491–8504. 2449
- 2392 44. Kietzmann T. Metabolic zonation of the liver: the oxygen 2450
- 2393 gradient revisited. *Redox Biol* 2017;11:622–630. 2451
- 2394 45. Halpern KB, Shenhav R, Matcovitch-Natan O, Toth B, 2452
- 2395 Lemze D, Golan M, Massasa EE, Baydatch S, Landen S, 2453
- 2396 Moor AE, Brandis A, Giladi A, Avihail AS, David E, Amit I, 2454
- 2397 Itzkovitz S. Single-cell spatial reconstruction reveals 2455
- 2398 global division of labour in the mammalian liver. *Nature 2456*
- 2399 2017;542:352–356. 2457
- 2400 46. Macpherson AJ, Heikenwalder M, Ganai-Vonarburg SC. 2458
- 2401 The liver at the nexus of host-microbial interactions. *Cell 2459*
- 2402 Host Microbe 2016;20:561–571. 2460
- 2403 47. Shao W, Espenshade PJ. Expanding roles for SREBP in 2461
- 2404 metabolism. *Cell Metab* 2012;16:414–419. 2462
- 2405 48. Meng Z, Liu N, Fu X, Wang X, Wang Y, Chen W, Zhang L, 2463
- 2406 Forman BM, Huang W. Insufficient bile acid signaling 2464
- 2407 impairs liver repair in CYP27^{-/-} mice. *J Hepatol* 2011; 2465
- 2408 55:885–895. 2466
- 2409 49. Pratt-Hyatt M, Lickteig AJ, Klaassen CD. Tissue distri- 2467
- 2410 bution, ontogeny, and chemical induction of aldo-keto 2468
- 2411 reductases in mice. *Drug Metab Dispos* 2013; 2469
- 2412 41:1480–1487. 2470
- 2413 50. Herrema H, Meissner M, van Dijk TH, Brufau G, 2471
- 2414 Boverhof R, Oosterveer MH, Reijngoud D-J, Müller M, 2472
- 2415 Stellaard F, Groen AK, Kuipers F. Bile salt sequestration 2473
- 2416 induces hepatic de novo lipogenesis through farnesoid X 2474
- 2417 receptor- and liver X receptor α -controlled metabolic 2475
- 2418 pathways in mice. *Hepatology* 2010;51:806–816. 2476
51. Nikolaou N, Gathercole LL, Marchand L, Althari S, 2420
- Dempster NJ, Green CJ, van de Bunt M, McNeil C, 2421
- Arvaniti A, Hughes BA, Sgromo B, Gillies RS, 2422
- Marschall H-U, Penning TM, Ryan J, Arlt W, Hodson L, 2423
- Tomlinson JW. AKR1D1 is a novel regulator of metabolic 2424
- phenotype in human hepatocytes and is dysregulated in 2425
- non-alcoholic fatty liver disease. *Metabolism* 2019; 2426
- 99:67–80. 2427
52. Thekkinghat AA, Yadav KK, Rangarajan PN. Apolipo- 2428
- protein L9 interacts with LC3/GABARAP and is a 2429
- microtubule-associated protein with a widespread sub- 2430
- cellular distribution. *Biol Open* 2019;8:bio045930. 2431
53. Snyder JM, Zhong G, Hogarth C, Huang W, Topping T, 2432
- LaFrance J, Palau L, Czuba LC, Griswold M, Ghiaur G, 2433
- Isoherranen N. Knockout of Cyp26a1 and Cyp26b1 2434
- during postnatal life causes reduced lifespan, dermatitis, 2435
- splenomegaly, and systemic inflammation in mice. 2436
- FASEB J* 2020;34:15788–15804. 2437
54. Pavlović N, Goločorbin-Kon S, Đanić M, Stanimirov B, 2438
- Al-Salami H, Stankov K, Mikov M. Bile acids and their 2439
- derivatives as potential modifiers of drug release and 2440
- pharmacokinetic profiles. *Front Pharmacol* 2018;9:1283. 2441
55. Zou Y, Bao Q, Kumar S, Hu M, Wang G-Y, Dai G. Four 2442
- waves of hepatocyte proliferation linked with three waves 2443
- of hepatic fat accumulation during partial hepatectomy- 2444
- induced liver regeneration. *PLoS One* 2012;7:e30675. 2445
56. Brasaemle DL. Cell biology: enhanced: a metabolic push 2446
- to proliferate. *Science* 2006;313:1581–1582. 2447
57. Huang W. Nuclear receptor-dependent bile acid 2448
- signaling is required for normal liver regeneration. *Sci- 2449*
- ence* 2006;312:233–236. 2450
58. Takaki Y, Hirai S, Manabe N, Izumi Y, Hirose T, 2451
- Nakaya M, Suzuki A, Mizuno K, Akimoto K, Tsukita S, 2452
- Shuin T, Ohno S. Dynamic changes in protein compo- 2453
- nents of the tight junction during liver regeneration. *Cell 2454*
- Tissue Res* 2001;305:399–409. 2455
59. Naugler WE. Bile acid flux is necessary for normal liver 2456
- regeneration. *PLoS One* 2014;9:e97426. 2457
60. Uriarte I, Fernandez-Barrena MG, Monte MJ, Latasa MU, 2458
- Chang HCY, Carotti S, Vespasiani-Gentilucci U, 2459
- Morini S, Vicente E, Concepcion AR, Medina JF, 2460
- Marin JGG, Berasain C, Prieto J, Avila MA. Identification 2461
- of fibroblast growth factor 15 as a novel mediator of liver 2462
- regeneration and its application in the prevention of 2463
- post-resection liver failure in mice. *Gut* 2013;62:899–910. 2464
61. Pereyra D, Starlinger P. Shaping the future of liver sur- 2465
- gery: Implementation of experimental insights into liver 2466
- regeneration. *Eur Surg* 2018;50:132–136. 2467
62. Ahmed N, Vernick JJ. Management of liver trauma in 2468
- adults. *J Emerg Trauma Shock* 2011;4:114–119. 2469
63. Zhang P, Wang S, Wang S, Qiao J, Zhang L, Zhang Z, 2470
- Chen Z. Dual function of partitioning-defective 3 in the 2471
- regulation of YAP phosphorylation and activation. *Cell 2472*
- Discovery* 2016;2:16021. 2473
64. Sourisseau T, Georgiadis A, Tsapara A, Ali RR, Pestell R, 2474
- Matter K, Balda MS. Regulation of PCNA and cyclin D1 2475
- expression and epithelial morphogenesis by the ZO-1- 2476

- 2477 regulated transcription factor ZONAB/DbpA. *Mol Cell Biol* 2006;26:2387–2398.
- 2478
- 2479 65. Huerta M, Muñoz R, Tapia R, Soto-Reyes E, Ramírez L,
2480 Recillas-Targa F, González-Mariscal L, López-
2481 Bayghen E. Cyclin D1 is transcriptionally down-regulated
2482 by ZO-2 via an E box and the transcription factor c-Myc.
2483 *Mol Biol Cell* 2007;18:4826–4836.
- 2484 66. Nava P, Capaldo CT, Koch S, Kolegraaf K, Rankin CR,
2485 Farkas AE, Feasel ME, Li L, Addis C, Parkos CA,
2486 Nusrat A. JAM-A regulates epithelial proliferation
2487 through Akt/ β -catenin signalling. *EMBO Rep* 2011;
2488 12:314–320.
- 2489 67. Loforese G, Malinka T, Keogh A, Baier F, Simillion C,
2490 Montani M, Halazonetis TD, Candinas D, Stroka D.
2491 Impaired liver regeneration in aged mice can be rescued
2492 by silencing Hippo core kinases MST1 and MST2. *EMBO*
2493 *Mol Med* 2017;9:46–60.
- 2494 68. van Dijk D, Sharma R, Nainys J, Yim K, Kathail P,
2495 Carr AJ, Burdziak C, Moon KR, Chaffer CL,
2496 Pattabiraman D, Bierie B, Mazutis L, Wolf G,
2497 Krishnaswamy S, Pe'er D. Recovering gene interactions
2498 from single-cell data using data diffusion. *Cell* 2018;
2499 174:716–729.e27.
- 2500 69. Deutsch MJ, Schriever SC, Roscher AA, Ensenaer R.
2501 Digital image analysis approach for lipid droplet size
2502 quantitation of Oil Red O-stained cultured cells. *Anal*
2503 *Biochem* 2014;445:87–89.
- 2504 70. Febres-Aldana CA, Alghamdi S, Krishnamurthy K,
2505 Poppiti RJ. Liver fibrosis helps to distinguish autoim-
2506 mune hepatitis from DILI with autoimmune features: a
2507 review of twenty cases. *J Clin Transl Hepatol* 2019;
2508 7:21–26.
- 2509 71. Schindelin J, Arganda-Carreras I, Frise E, Kaynig V,
2510 Longair M, Pietzsch T, Preibisch S, Rueden C,
2511 Saalfeld S, Schmid B, Tinevez J-Y, White DJ,
2512 Hartenstein V, Eliceiri K, Tomancak P, Cardona A. Fiji: an
2513 open-source platform for biological-image analysis. *Nat*
2514 *Methods* 2012;9:676–682.
- 2515 72. Odriozola A, Llodrá J, Radecke J, Ruegsegger C,
2516 Tschanz S, Saxena S, Rohr S, Zuber B. High contrast
2517 staining for serial block face scanning electron micro-
2518 scopy without uranyl acetate. *bioRxiv*
- 2519 73. Chihara M, Ikebuchi R, Otsuka S, Ichii O, Hashimoto Y,
2520 Suzuki A, Saga Y, Kon Y. Mice stage-specific claudin 3
2521 expression regulates progression of meiosis in early
2522 stage spermatocytes. *Biol Reprod* 2013;89:3.
- 2523 74. Yates AD, Achuthan P, Akanni W, Allen J, Allen J,
2524 Alvarez-Jarreta J, Amode MR, Armean IM, Azov AG,
2525 Bennett R, Bhai J, Billis K, Boddu S, Marugán JC,
2526 Cummins C, Davidson C, Dodiya K, Fatima R, Gall A,
2527 Giron CG, Gil L, Grego T, Haggerty L, Haskell E,
2528 Hourlier T, Izuogu OG, Janacek SH, Juettemann T,
2529 Kay M, Lavidas I, Le T, Lemos D, Martinez JG, Maurel T,
2530 McDowall M, McMahon A, Mohanan S, Moore B,
2531 Nuhn M, Ohen DN, Parker A, Parton A, Patricio M,
2532 Sakthivel MP, Abdul Salam AI, Schmitt BM,
2533 Schuilenburg H, Sheppard D, Sycheva M, Szuba M,
2534 Taylor K, Thormann A, Threadgold G, Vullo A, Walts B,
2535 Winterbottom A, Zadissa A, Chakiachvili M, Flint B,
2536 Frankish A, Hunt SE, Ilesley G, Kostadima M, Langridge N,
2537 Loveland JE, Martin FJ, Morales J, Mudge JM,
2538 Muffato M, Perry E, Ruffier M, Trevanion SJ,
2539 Cunningham F, Howe KL, Zerbino DR, Flicek P. Ensembl
2540 2020. *Nucleic Acids Res* 2020;48:D682–D688.
- 2541 75. Kim D, Paggi JM, Park C, Bennett C, Salzberg SL.
2542 Graph-based genome alignment and genotyping with
2543 HISAT2 and HISAT-genotype. *Nat Biotechnol* 2019;
2544 37:907–915.
- 2545 76. Li H, Handsaker B, Wysoker A, Fennell T, Ruan J,
2546 Homer N, Marth G, Abecasis G, Durbin R. The sequence
2547 alignment/Map format and SAMtools. *Bioinformatics*
2548 2009;25:2078–2079.
- 2549 77. Liao Y, Smyth GK, Shi W. FeatureCounts: an efficient
2550 general purpose program for assigning sequence reads
2551 to genomic features. *Bioinformatics* 2014;30:923–930.
- 2552 78. Love MI, Huber W, Anders S. Moderated estimation of
2553 fold change and dispersion for RNA-seq data with
2554 DESeq2. *Genome Biol* 2014;15:550.
- 2555 79. Zhu A, Ibrahim JG, Love MI. Heavy-tailed prior distribu-
2556 tions for sequence count data: removing the noise and
2557 preserving large differences. *Bioinformatics* 2019;
2558 35:2084–2092.
- 2559 80. Zhou Y, Zhou B, Pache L, Chang M, Khodabakhshi AH,
2560 Tanaseichuk O, Benner C, Chanda SK. Metascape pro-
2561 vides a biologist-oriented resource for the analysis of
2562 systems-level datasets. *Nat Commun* 2019;10:1523.
- 2563 81. Gómez C, Stücheli S, Kratschmar DV, Bouitbir J,
2564 Odermatt A. Development and validation of a highly
2565 sensitive LC-MS/MS method for the analysis of bile
2566 acids in serum, plasma, and liver tissue samples. *Me-
2567 tabolites* 2020;10:282.
- 2568 82. Penno CA, Arsenijevic D, Da Cunha T, Kullak-Ublick GA,
2569 Montani J-P, Odermatt A. Quantification of multiple bile
2570 acids in uninephrectomized rats using ultra-performance
2571 liquid chromatography-tandem mass spectrometry. *Anal*
2572 *Methods* 2013;5:1155.

Received August 18, 2020. Accepted April 6, 2021.

Correspondence

Address correspondence to: Deborah Stroka, MD, Murtenstrasse 35, 3008 Bern, Switzerland. e-mail: deborah.stroka@dbmr.unibe.ch; fax: (41) xxx-xxxx.

Acknowledgements

CRedit Authorship Contributions

Felix Alexander Baier, PhD (Conceptualization: Supporting; Data curation: Lead; Formal analysis: Lead; Investigation: Equal; Methodology: Lead; Visualization: Lead; Writing – original draft: Equal; Writing – review & editing: Equal)

Daniel Sánchez-Taltavull, PhD (Formal analysis: Supporting; Methodology: Supporting; Software: Supporting; Validation: Supporting; Visualization: Supporting; Writing – review & editing: Supporting)

Tural Yarahmadov, PhD (Formal analysis: Supporting; Methodology: Supporting; Software: Supporting; Validation: Supporting; Visualization: Supporting; Writing – review & editing: Supporting)

Cristina Gómez Castellà, PhD (Formal analysis: Supporting; Methodology: Supporting; Resources: Supporting; Validation: Supporting)

Fadi Jebbawi, PhD (Formal analysis: Supporting; Methodology: Supporting; Resources: Supporting; Software: Supporting; Validation: Supporting)

Adrian Keogh, PhD (Methodology: Supporting; Resources: Supporting; Validation: Supporting; Writing – review & editing: Supporting)

Riccardo Tombolini, - (Methodology: Supporting; Resources: Supporting)

Adolfo Odriozola, - (Methodology: Supporting; Resources: Supporting)

Mariana Castro Dias, PhD (Resources: Supporting)

Urban Deutsch, PhD (Resources: Supporting; Writing – review & editing: Supporting)

Mikio Furuse, Prof (Resources: Supporting)

2595	Britta Engelhardt, Prof (Funding acquisition: Supporting; Resources: Supporting; Writing – review & editing: Supporting)	2612
2596	Benoît Zuber, Prof (Funding acquisition: Supporting; Resources: Supporting; Writing – review & editing: Supporting)	2613
2597	Alex Odermatt, Prof (Funding acquisition: Supporting; Resources: Supporting; Writing – review & editing: Supporting)	2614
2598	Daniel Candinás, Prof (Funding acquisition: Supporting)	2615
2599	Deborah Stroka, Prof (Conceptualization: Lead; Formal analysis: Supporting; Funding acquisition: Lead; Investigation: Equal; Project administration: Lead; Resources: Supporting; Supervision: Lead; Validation: Lead; Writing – original draft: Equal; Writing – review & editing: Equal)	2616
2600	The authors thank the Next Generation Sequencing platform at the University of Bern for their technical assistance with the RNAseq experiments. The authors also would like to acknowledge Carlos Wotzkow and Dr Fabian Blank from the Live Cell Imaging facility in Bern for their assistance with microscopy. Light and electron microscopy were performed on devices	2617
2601		2618
2602		2619
2603		2620
2604		2621
2605		2622
2606		2623
2607		2624
2608		2625
2609		2626
2610		2627
2611		2628

Conflicts of interest

The authors disclose no conflicts.

Funding

Supported by SNF grant 173157 (D.S.), The European Union Seventh Framework Program FP7 under grant agreements 241861 (JUSTBRAIN) and 607962 (nEUROinflammation), and SNF grants 189080 (B.E.), 179520 (B.Z.), and 179400 (A.I.O.).

UNCORRECTED PROOF